Master's thesis

NTNU
Norwegian University of Science and Technology
Faculty of Engineering
Department of Energy and Process Engineering

Rebekka Jennings Stjern

Numerical study of particle settlement in a sand trap with multiple flow calming structures

Master's thesis in Mechanical Engineering
Supervisor: Chirag Trivedi
June 2023

NTNU
Norwegian University of
Science and Technology

Rebekka Jennings Stjern

Numerical study of particle settlement in a sand trap with multiple flow calming structures

Master's thesis in Mechanical Engineering
Supervisor: Chirag Trivedi
June 2023

Norwegian University of Science and Technology
Faculty of Engineering
Department of Energy and Process Engineering

NTNU
Norwegian University of
Science and Technology

Waterpower Laboratory

NTNU

Abstract

A traditional sand trap within a hydropower plant reduces flow velocity, enabling transported sediments to separate from the water. Optimizing sediment deposition is crucial to minimize turbine erosion caused by particles, making the research of flow calming structures and ribs interesting. Previous research has studied particle behavior concerning hydropower, although achieving a definitive optimization for a sand trap remains to be established. The study aims to investigate flow and sand particle behavior upon impact with flow calming structures and ribs to comprehend particle behavior better downstream of these objects. Simplified sand trap models were developed, containing single and multiple cylinders of varied geometries representing flow calming structures. The models were discretized and verified before progressing to performing the numerical simulations. The flows were simulated for a transient state, using Reynolds-averaged Navier-Stokes turbulence models to solve the equations.

The results demonstrate that the particles, hence smaller and suspended sediments in a hydropower plant, closely follow the flow pattern. Additionally, the particle behavior is affected by gravitational forces and the flow's inertial forces. In the case of a single flow calming structure, the model containing a circular cylinder proved to contribute to particle settlement due to more particles entering the ribs upstream of the outlet. For the case of multiple flow calming structures, the model containing square cylinders proved advantageous, based on a smoother pattern being more beneficial. Fewer velocity fluctuations allow particles to have trajectories following the streamlines constantly.

Keywords: Hydropower; Sand trap; CFD; Sediment transport; Multiphase;

Vannkraftlaboratoriet

NTNU

Sammendrag

Et tradisjonelt sandfang i et vannkraftverk reduserer strømningshastigheten slik at sedimenter som transporteres kan skilles ut fra vannet. For å minimere turbinerosjon forårsaket av partikler er det nødvendig å optimere sedimentavsetningen i sandfanget, noe som gir interesse for videre forskning på strukturer og ribber. Det har tidligere blitt utført forskning av partikkelavsetning i relasjon med vannkraft, men et sandfang med optimal avsetning er enda ikke etablert. Denne studien har som mål å undersøke strømnings-og partikkelatferd når sandfanget har installerte strukturer og ribber, noe som gir bedre forståelse av partikkelavsettelse nedstrøms disse objektene. Forenklede modeller av sandfang er utviklet, og inneholder både én og flere sylindre av ulike geometrier, som representerer strukturene. Modellene er diskretisert og verifisert før de numeriske simuleringene er utført. Strømningene er simulert for en transient tilstand ved bruk av Reynolds-averaged Navier-Stokes turbulensmodeller for å løse ligningene.

Resultatene viser at partiklene, og dermed de mindre og suspenderte sedimentene i et vannkraftverk, følger strømningsmønsteret tett. I tillegg påvirkes partiklene av gravitasjonskrefter og treghetskrefter fra strømnignen. I tilfellet med én struktur viste resultatene at modellen med en sirkulær sylinder bidrar mest til økt partikkelavsetning, på grunn av bedre opphopning av partikler under ribbene. I tilfellet med flere strukturer viste resultatene at kvadratiske sylindre er bedre egnet, basert på et jevnere strømningsmønster. Færre hastighetssvingninger bidrar til at partiklene følger strømningslinjene til vannet mer kontinuerlig, noe som gjør et jevnere strømningsmønster gunstigere for partikkelavsetning.

Acknowledgments

I sincerely thank my supervisor, Associate Professor Chirag Trivedi, for his guidance, expertise, and support throughout this project. His constructive feedback, insights, and availability for questions have been very valuable and are much appreciated. I am also grateful for being granted access to the supercomputers Aura and IDUN, providing sufficient computational resources for the project to unfold.

My deepest and heartfelt gratitude goes to my family and friends for their unconditional support. Their encouragement, understanding, and belief in my abilities have been invaluable motivation sources during the challenging and rewarding moments of my journey at NTNU.

I would also like to thank the administration, PhD candidates, and fellow students at the Waterpower Laboratory. The facilities, social arrangements, teamwork, and journeys shared have made the study year incredibly memorable and great.

Contents

List of tables

List of figures

Nomenclature

Abbreviation

APG	Adverse pressure gradient
CAD	Computer-aided design
CFD	Computational fluid dynamics
DNS	Direct numerical simulation
DPM	Discrete phase model
FCS	Flow calming structure
GCI	Grid convergence index
LES	Large eddy simulation
NTNU	Norwegian University of Science and Technology
RANS	Reynolds-averaged Navier-Stokes
SAS	Scale-adaptive simulation
SST	Shear stress transport

Latin symbols

a	Wall width (m)
A	Area (m^2)
a_1	Constant

C_d	Drag coefficient
C_l	Lift coefficient
C_μ	Constant
D	Diameter (m)
D_h	Hydraulic diameter (m)
F_d	Drag force (kg m s^{-2})
F_l	Lift force (kg m s^{-2})
g	Gravitational acceleration (m s^{-2})
I	Turbulence intensity
k	Turbulent kinetic energy (m^2 s^{-2})
ℓ	Perimeter (m)
L	Length scale (m)
$\dot{m}$	Mass flow rate (kg s^{-1})
p	Total pressure (kg m^{-1} s^{-2})
Q	Flow rate (m^3 s^{-1})
S	First velocity gradient
t	Time (s)
U	Free stream velocity (m s^{-1})
U''	Second velocity gradient
u_m	Mean velocity (m s^{-1})
u	Peripheral velocity (m s^{-1})
u^*	Shear velocity (m^{-1})
u'	Velocity fluctuation (m s^{-1})
w_0	Settling velocity (m s^{-1})
W	Slip velocity (m s^{-1})

y^+ Ratio parameter

Dimensionless numbers

Re Reynolds number

Stk Stokes number

Greek symbols

β Constant

γ Constant

δ Kroenecker-delta

ϵ Turbulent dissipation rate (m^2 s^{-3})

η Trap efficiency (%)

μ Dynamic viscosity (kg m^{-1} s^{-1})

ν Kinematic viscosity (kg m^{-1} s^{-1})

ν_T Kinematic eddy viscosity (kg m^{-1} s^{-1})

ϕ Pressure head loss (N m^{-2})

ρ Density (kg m^{-3})

τ Reynolds stress tensor

ω Specific dissipation rate (s^{-1})

ξ Constant

Superscripts and subscripts

1D One dimensional

3D Three dimensional

c Circular

f Fluid

i,j Indices

k Kinetic energy

p	Particle
s	Square
t	Tunnel
vK	von Kármán
ω	Dissipation rate

Chapter 1

Introduction

1.1 Background

Hydropower has gained significant interest as a renewable energy resource that harnesses natural water flow energy. Hydropower plants are strategically located near water resources, utilizing turbines and generators to convert the kinetic energy of water to electricity. Figure 1.1 illustrates the main components in a typical impoundment hydropower plant. In such a power plant, the water is extracted from an upper reservoir or dam, with additional brook intakes to utilize water from smaller resources. The water from these intakes will further meet and flow through a headrace tunnel. Downstream the headrace tunnel, a surge tank, and a sand trap are positioned. The surge tank neutralizes the system's pressure before the water enters the sand trap, where the sediments settle. The water continues through the penstock, where the head naturally increases, and subsequently flows through the turbine house, powering the turbines. Throughout this process, the kinetic energy of the water is converted into electrical energy by generators, after which the flow is released into a lower reservoir or river.

Sand traps are essential components in hydropower plants, optimizing production by indirectly reducing turbine damage. Two types of sand traps are open channel and closed tunnel sand traps. A distinction between these two types lies in the surface orientations that confine the flow. In an open channel, the flow is confined by the channel bed and side walls, while in a closed tunnel, the flow is enclosed by the tunnel bed, side walls, and roof. Both types are located upstream of the penstock and have a wider cross-sectional area than the headrace tunnel, reducing water velocity upon entry. The velocity decrease allows the sediments to settle at the bed by reaching their settling velocity.

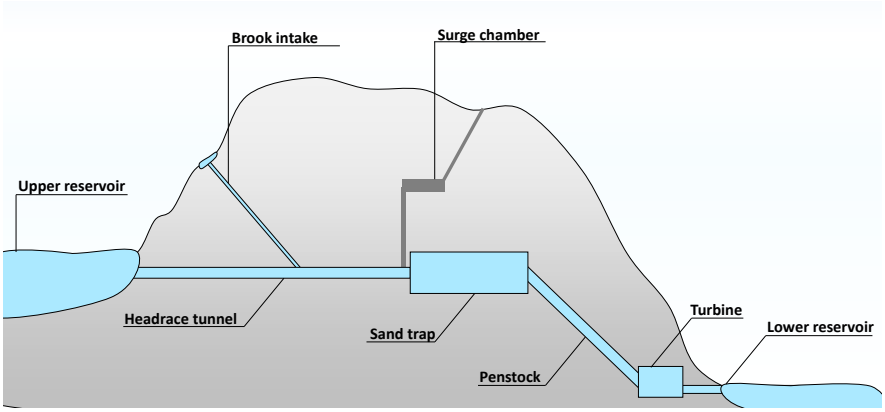

Figure 1.1: Illustration of an impoundment hydropower plant, with the main features prominently highlighted for identification.

The closed tunnel sand trap, also called a pressurized sand trap, is beneficial in an impoundment hydropower plant as it captures particles from various sources, including the headrace tunnel, brook intakes, unlined channels, and sediments remaining from construction [1]. Factors such as the water intake source, location, sediment types, and cost influence the installation of sand traps.

Sediments transported with incoming water pose challenges to achieving optimal production in hydropower plants. Several factors, including the intake source, sediment type and size, water velocity, and turbulence levels, influence the quantity of transported sediments. Over time, the unsettled deposits cause erosion damage to the turbines, reducing operational life and resulting in maintenance and replacement operations downtime. These factors cause the hydropower plant to have reduced electricity production, leading to decreased efficiency. To address this issue, sand traps have been designed and installed in hydropower plants to minimize the transport of sediments to the penstock and turbines, thereby increasing efficiency. Upgrading sand traps with designs that capture more sediments allows the turbines to operate more constantly and have an extended lifespan. Given the current relevance of renewable energy resources, optimizing the design of hydropower sand traps is essential for maximizing power production.

1.2 Scope

This master's work builds upon a previous project focused on understanding hydropower and exploring flow behavior using numerical tools [2]. Because the current study continues this previous project, certain similarities will be observed in the theory. The earlier project employed a simplified sand trap model featuring a tunnel with a single vertical, square cylinder positioned downstream of the tunnel inlet. The investigations involved multiphase one-way coupled simulations examining the flow and particle dynamics when encountering the obstruction. The results showed that particles were trapped in the outer regions of vortices, causing them to follow the pattern of the growing vortices. As the vortices expanded, the flow velocity decreased, reducing the particles' velocity. It was found that the tunnel length should be increased for future work, and it would be necessary to perform fully-coupled simulations to investigate the particles' effect on each other or the flow.

The present study aims to investigate how different structures will affect the water flow and sediment settlement inside a sand trap. A numerical analysis will be conducted to observe flow behavior as it interacts with structures of varying geometries. The created models are tunnels containing a single vertical cylinder, a single circular cylinder, and multiple cylinders located downstream of the tunnel inlets. Upon flow stabilization, particles will be injected, making it possible to study their physical tendencies. Specific models are additionally conducted with a second inlet velocity to observe how turbulence affects the particle settlement.

1.3 Thesis organization

In this section, the structure of the thesis will be outlined. The initial step involved conducting a literature study to gather previous knowledge about flow properties and acquire valuable insight considering the physical aspects of particle settlement. The literature review includes results and conclusions of relevant research, as well as summaries of projects of relevance for decisions made in this study.

Furthermore, the thesis will present the relevant theoretical foundations needed, such as sediment transportation methods. Subsequently, the thesis will delve into the theory concerning specific flow phenomena and turbulence, followed by CFD theory and model verification. Chapter 3 ends the applied

simulation setup.

In Chapter 4, the results for this study are obtained. The results will be presented and discussed regarding the matter in question and the relevant literature. The conclusions from the results are to be found in Chapter 5, followed by suggestions for future work in Chapter 6.

Chapter 2

Literature review

The settling behavior of particles in water is a critical aspect to consider in hydropower plants, and previous research studies have yielded varying results. While investigating the motion of aerosol particles in a steady flow, Maxey and Corrsin [3] discovered that particles have indefinite suspension if no inertial forces are present. In contrast, if inertial forces are present, the particles are settled at a higher rate than in still fluid. Regarding turbulence affecting the particle settlement, Nielsen [4] observed that bubbles tend to be trapped inside steady vortices while heavy particles escape. A density difference between the bubbles and the particles causes a transportation difference, leading heavy particles to become fast-tracked between the vortices. This phenomenon led the settling velocity to become reduced by weak turbulence and increased by strong turbulence. The observed bubble and particle behavior regards a horizontal flow as the density leads to a gravity pull impacting their velocity if the flow model is declined or inclined. Nielsen's results correspond to the discoveries of Maxey and Corrsin [3], which suggests that it is crucial to investigate the particle and vortex interaction at a deeper level. In terms of already settled particles, Ingersoll et al. [5] discovered that an essential factor in preventing settled particles' re-suspension was to have small velocity gradients at the tunnel bed. These findings align with Nielsen [4], as increased turbulence levels are associated with higher velocities.

Murray [6] observed that the particle settlement velocity was reduced by 30% compared to the still-water fall velocity while conducting experimental studies on suspended particles. By performing DNS on particle-laden flows, Wang and Maxey [7] found that the settling velocity can increase up to 50% when the particles have an inertial response time and still-fluid terminal velocity comparable to the Kolmogorov turbulence scales.

Wang and Squires [8] conducted a numerical study to investigate the deposition of particles in a fully-developed turbulent flow. The conclusions were that the particles accumulated in the near-wall region of the boundary layer, based on both LES and DNS. In order to characterize the particle interactions while settling, Liu et al. [9] conducted a study with experiments and simulations. While Menter [10] neglected the particle-particle interactions, Liu et al. [9] included these in the study. The results showed no attraction between particles released side by side but rather a repulsion caused by the asymmetry between the inside and outside vortices in the wake.

Researchers have conducted various studies investigating turbulence induced by particles. Kajishima and Takiguchi [11] performed DNS in order to investigate the two-way interaction between particles and a level of turbulence in a fluid. The results indicated that the clusters increased when the particle Reynolds number exceeded 300, and a higher amount of particle clusters created a reduced drag induced by the particles. The increase in cluster formation is due to the drag created by a particle being lower if the particle is in a wake from another particle rather than in a free stream. The results also showed that clusters induced large-scale eddies into the flow. Burton and Eaton conducted another numerical fully-coupled study [12], where the results showed that the ratio of particle mass load to fluid is of essence to the level of turbulence. Results indicate that systems with higher mass loads have reduced turbulence levels from their unladen values. In contrast, a small mass load can increase turbulence from their unladen values.

In the present study, it is interesting to investigate the flow and particle behaviour as it passes by an obstacle. Burns et al. [13] found that particles will concentrate near the edges of the vortices downstream of a bluff body. Here, an attraction occurs between the particles due to dissipative effects caused by particle inertia in the flow. Haddadi et al. [14] looked into the behaviour of particles in recirculating wakes. The results show that a steady and unsteady wake differs due to the occurring mass exchange in an unsteady flow. A single particle injection into the free stream does not enter the wake. In contrast, with a more significant particle injection, the particles will move across the wake and enter the free stream.

Khosronejad et al. [15] used three-dimensional simulations to investigate a flow with sediments. The low-Reynolds number k-ω turbulence model and a standard k-ϵ turbulence model were applied for the numerical solver, which both are based on the Boussinesq eddy viscosity hypothesis. The result showed that the low-Reynolds k-ω model predicts the multiphase flow better than the standard k-ϵ model. The results of Khosronejad et al. [15] agree

with the theory of the k-ω model, as it accounts better for the layers in the near-wall region, while the k-ϵ model is more applicable in the free-stream region [16]. The different application regions of the two turbulence models are due to the empirical damping functions that k-ϵ uses in the viscous sub-layer for a low y^+ value, which the k-ω turbulence model does not include. Menter [10] presented two turbulence models, the Baseline and SST models, in which he compared their accuracy. The two models were comparable because they were based on the k-ω model and two-equation eddy viscosity models. It was found that the two models showed differences in the free stream part of the boundary layer, where the SST model became favourable. The SST model was favourable because it had less sensitivity in this region, compared to the original k-ω and the Baseline model, due to a modification in the definition of the eddy-viscosity. Hence, it accounts for the turbulent shear stress in the flow.

This master study is based on the research conducted by Ivarson [17] and Daving [18]. Ivarson investigated the effects on sand trap efficiency when installing v-shaped rakes and ribs in the sand trap through a numerical study. The model was a realistic sand trap design with two rows of rakes downstream of the sand trap inlet. The rows consisted of 11 and 12 rakes, which did not extend to the channel's top. Results showed that when including the ribs, the number of sediments that escaped was reduced by 24% and the head loss was increased by 1.8%, while when including both ribs and rakes, the amount was increased by 48.5% and 12.7%, respectively. For further work, it was suggested that models should include rakes extending across the entire tunnel, and acquiring experimental measurements of the inlet velocity would be necessary for accurate boundary conditions.

Further numerical investigations into the sand trap design were conducted by Daving [18]. The scope of the study was to observe the effects on sand trap efficiency when installing square and diamond-shaped rakes, so-called Flow Calming Structures, and ribs, while also having an incline and decline in the tunnel. A set of models were created to explore the various cases of particle settlement. The results for a pressurized channel concluded that including FCS decreased particle settlement by 30% from the results without FCS. The case for an open channel resulted in a decrease of 34% from the original case. An inclined tunnel downstream of the sand trap gave a settlement of 31%, which is lower than the beforementioned results. It was suggested that future work should include a closer look at the vortex and particle interaction, as well as optimizing the models to reduce simulation time.

Næss [19] and Steinkjer [20] also conducted studies regarding particle injections for a sand trap. Næss [19] performed numerical simulations with a realistic sand trap design consisting of both an open and closed sand trap. The results showed that flow velocity is reduced at the tunnel bed, giving better conditions for particle settlement. Steinkjer [20] conducted a physical lab experiment to investigate the best-suited modelling material for future sand trap experiments. The parameters from the work of Næss [19], Steinkjer [20], Ivarson [17] and Daving [18], in which the current study is based on, are presented in Table 2.1.

Table 2.1: Case parameters from previous related studies regarding particle settlement.

Parameter		Daving [18]	Ivarson [17]	Næss [19]	Steinkjer [20]
A_c	[m^2]	1.10×10^{2}	1.19×10^{2}	3.39×10^{2}	3.30×10^{-1}
D_p	[m]	2.00×10^{-4}	(7.50 ± 2.50)	3.00×10^{-4}	2.5×10^{-4}
		2.0×10^{-3}	$\times10^{-4}$	1.00×10^{-3}	4.9×10^{-4}
ρ_p	[kg m^{-3}]	1.60×10^{3}		2.65×10^{3}	2.62×10^{3}
Q_p	[kg s^{-1}]	2.00×10^{-2}	1.00×10^{3}	1.00	
t_p	[s]	1.00×10^{2}	1.00×10^{2}	2.00×10^{1}	5.60×10^{3}
m_p	[kg]	2.00	1.00×10^{5}	2.00×10^{1}	1.97×10^{2}
$D_{h,c}$	[m]	1.05×10^{1}	1.05×10^{1}		5.74×10^{-1}
$D_{h,FCS}$	[m]	2.20×10^{-1}	2.00×10^{-1}		
U_{in}	[m s^{-1}]	1.14	1.14	2.36	(0.8, 2.20) $\times10^{-1}$
Re		1.15×10^{7}	1.15×10^{-7}		4.60×10^{4}

Here, A_c is the cross-sectional area of the channel and tunnel, D_p is the particle diameter, ρ_p is the particle density, Q_p is the particle injection flow rate, t_p is the injection time, m_p is the total injected particle mass, $D_{h,c}$ is the hydraulic channel and tunnel diameter, $D_{h,FCS}$ is the hydraulic diameter of the FCS, U_{in} is the inlet velocity and Re is the flow Reynolds number. A lack of consistency was observed for the previous studies, resulting in the present study creating parameters primarily based on parameters from Daving [18]. This choice was made because it was the case most related to the current case. Therefore, the parameters used in this study are presented in Table 2.2.

Table 2.2: Case parameters and their values for the models considered.

Parameter		$U_{in} = 1.5$ m s^{-1}		$U_{in} = 15$ m s^{-1}	
		M_1,M_2,M_4	M_3,M_5	M_1,M_2,M_4	M_3,M_5
A_c	[m^2]	5.00×10^{-3}	1.10×10^{-2}	5.00×10^{-3}	1.10×10^{-2}
D_p	[m]	2.00×10^{-4}	2.00×10^{-4}	2.00×10^{-4}	2.00×10^{-4}
ρ_p	[kg m^{-3}]	1.60×10^{3}		1.60×10^{3}	
Q_p	[kg s^{-1}]	9.00×10^{-7}		9.00×10^{-6}	
t_p	[s]	1.90		1.90×10^{-1}	
m_p	[kg]	1.71×10^{-6}		1.71×10^{-6}	
$D_{h,c}$	[m]	6.67×10^{-2}	1.05×10^{-1}	6.67×10^{-2}	1.05×10^{-1}
$D_{h,FCS}$	[m]	1.00×10^{-2}	1.00×10^{-2}	1.00×10^{-2}	1.00×10^{-2}
Re		1.00×10^{5}	1.50×10^{5}	1.00×10^{6}	1.50×10^{6}

In Table 2.2, M_1, M_2, M_3, M_4, and M_5 refer to Model 1, Model 2, Model 3, Model 4 and Model 5, respectively. These are the models created for this study, which will be presented in Chapter 3.5. The values for the particle injections arise from a down-scaling of the values from Table 2.1, while the structure measurements and inlet velocity are independently decided.

Chapter 3

Theory and methods

3.1 Sediment transport

Gaining a comprehensive understanding of sediments and their transportation by water is vital when examining the effectiveness of a sand trap. Sediments are composed of particles of different sizes, where the type of particle depends on the location and surrounding area of the hydropower plant [21]. The sediments are sorted into groups depending on their size, from small to large: clay, silt, sand, and gravel. The sediments come from the tunnel, both unlined and lined tunnels, or get transported from the waterways [20]. It is also common to leave remaining sediments after finished construction at the tunnel bed, causing them to get suspended as the water flows past. The sediments also originate from the concrete lining or rock support if there are lined tunnel walls. In addition, the sediments from waterways and brook intakes are transported through the headrace tunnel and to the sand trap. In the case of the primary intake being from a creek or river, the sediment concentration is expected to be higher than water from a reservoir due to the higher water velocity and increased erosion in natural waterways. However, an effective sand trap is crucial to minimize sediments reaching the penstock regardless of the water source.

The sediments and particles in the flow get transported by bed load or suspension load [21], as illustrated in Figure 3.1. Bed load transportation involves large sediments like sand, gravel, and boulders. Due to their mass, these get transported along the tunnel bed by sliding, rolling, and saltating. Sliding and rolling occurs directly at the tunnel bed, while saltating occurs when the sediment catches a re-suspension and is transported further downstream by the flow. The fluid motion transports smaller particles with suspension in the water, allowing them to deposit in the water as the flow

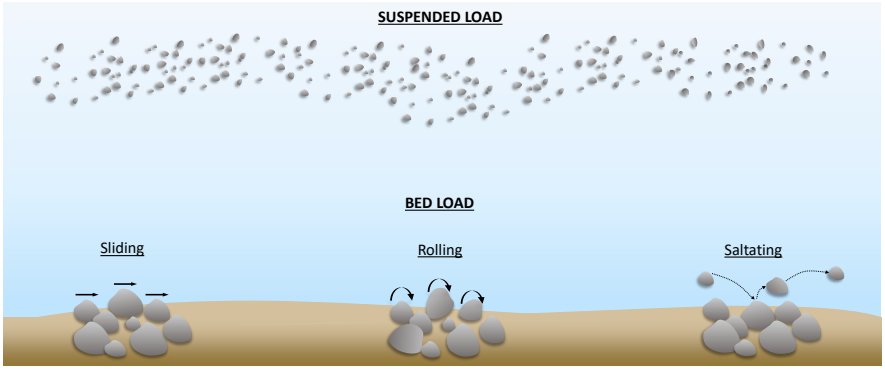

Figure 3.1: Illustration of sediment transportation methods occurring in a sand trap.

velocity reduces and they reach their settling velocity.

Suspension of a particle occurs when the shear velocity is greater than the particle settling velocity, hence $u^* > \omega_0$ [21]. The two parameters are given in Equation 3.1 and Equation 3.2, respectively.

$$u^* = \sqrt{\frac{\tau_0}{\rho}} \tag{3.1}$$

$$\omega_0 = -\sqrt{\frac{4gd_p}{3C_d}}\frac{\rho_p}{\rho} \tag{3.2}$$

Here, τ_0 is the bed shear stress, ρ is the fluid density, g is gravitational forces, d_p is the particle diameter, ρ_p is the particle density and C_d is the particle drag coefficient [22]. The drag coefficient for a spherical particle is given by Equation 3.3,

$$C_d = \frac{24}{Re_p}(1 + 0.150Re_p^{0.681}) + \frac{0.407}{1 + \frac{8710}{Re_p}} \tag{3.3}$$

where Re_p is the particle Reynolds number. The terminal fall velocity, also known as the settling velocity, of a particle in this study is $\omega_0 = 0.095$ m s^{-1}.

Different turbulence levels and FCS influence the tunnel flow by creating disturbances and vortices. The suspended particles follow the flow streamlines and hence the developed patterns. The Stokes number is dimensionless, indicating how coupled the particle motion is with the flow motion by being a ratio between the particle response time and the characteristic fluid time scale [23]. Equation 3.4 gives the Stokes number,

$$Stk = \frac{\rho_p d_p^2 U}{18 \mu L} \tag{3.4}$$

where U is the free stream velocity, μ is the fluid dynamic viscosity and L is the characteristic length scale for the vortex. A small Stokes number, $Stk << 1$, indicates that the motion of the suspended particles is highly coupled with the fluid motion, whereas a greater Stokes number, $Stk >> 1$, indicates that the particles behave in an independent matter [23]. The independent behavior of the particles is due to the particle having a response time to the incoming force that reacts faster than the fluid reacts on it, making the particle motion not related to the fluid motion.

Table 3.1 presents the Stokes numbers for the particles in the current study, where the values were obtained using Equation 3.4 and quantities from Table 2.2.

Table 3.1: Stokes numbers for the particle-laden flows in the models considered.

	Stokes number	
Model	$U_{in} = 1.5$ m s^{-1}	$U_{in} = 15$ m s^{-1}
M_1	7.97×10^{-2}	7.97×10^{-1}
M_2	7.97×10^{-2}	7.97×10^{-1}
M_3	5.06×10^{-2}	5.06×10^{-1}
M_4	7.97×10^{-2}	7.97×10^{-1}
M_5	5.06×10^{-2}	5.06×10^{-1}

The calculated values show that the tunnels with the same cross-sectional area induce the same Stokes number on the particles, as the tunnel hydraulic diameter is the reference length. The particles are closely coupled with the flow patterns in all cases because the Stokes number is less than 1.

3.2 Flow attributes

In a pressurized sand trap, the flow occurs internally within a tunnel. This flow type is characterized by a fluid confined by solid surfaces in all directions, except for the inlet and outlet [24]. The presence of solid surfaces leads to the development of a boundary layer and the importance of considering the viscous effects of the fluid in this region. Determining whether the flow is fully developed is crucial, considering turbulent flow conditions [25].

The current study includes flow past FCS, resulting in a flow past a cylinder. When the flow velocity, and hence the Reynolds number, is high, the cylinder detaches in the boundary layer, generating a flow separation at the cylinder walls [24]. This separation region forms a wake characterized by the periodic shedding of vortices, which is an unsteady phenomenon due to the flow's inherent time dependence. The frequency at which the vortices are shed is proportional to the average flow velocity, meaning higher velocities result in higher shedding frequencies. For flow over a cylinder, the lift and drag coefficients can be calculated using Equation 3.5 and Equation 3.6, respectively,

$$C_d = \frac{F_d}{0.5\rho U^2 A} \tag{3.5}$$

$$C_l = \frac{F_l}{0.5\rho U^2 A} \tag{3.6}$$

where F_d and F_l are the drag and lift forces acting on the cylinder and A is the cylinder area [24]. The flow separation in the boundary layer causes pressure differences that generate the drag force. These pressure differences create alternating high-pressure and low-pressure zones downstream of the cylinder, leading to a repeating formation of vortices, known as a von Kármán vortex street.

For the numerical analysis in this study, the hydraulic diameter is used as the characteristic length for the non-circular pipe, considering the rectangular cross-sectional area of the tunnel. The hydraulic diameter for the rectangular tunnel is calculated by Equation 3.7,

$$D_{h,t} = \frac{4A}{\ell} \tag{3.7}$$

where A_c is the cross-sectional area and ℓ is the wetted perimeter for

the tunnel. The hydraulic diameter of the cylinders differs from that of the rectangular tunnel. The hydraulic diameter for a square cylinder can be found in Equation 3.8, and for a circular cylinder, in Equation 3.9,

$$D_{h,s} = a \tag{3.8}$$

$$D_{h,c} = D \tag{3.9}$$

where a is the length of the cylinder walls and D is the cylinder diameter. The values found for the hydraulic diameters in this project can be viewed in Table 2.2. Due to the cylinders having equal hydraulic diameters, they are in Table 2.2 denoted $D_{h,FCS}$.

The Reynolds number is a dimensionless parameter representing a flow's turbulence level [24]. The fluid and particles have separate Reynolds numbers in a particle-laden flow. The Reynolds number for a fluid is determined using 3.10, while for a single particle, it is expressed by 3.11.

$$Re = \frac{\rho U D_h}{\mu} \tag{3.10}$$

$$Re_p = \frac{W d_p}{\nu_f} \tag{3.11}$$

Here, W is the magnitude of the slip velocity and ν_f is the kinematic viscosity of the surrounding fluid. While the fluid Re is a ratio of the inertial forces to the viscous forces, Re_p indicates a particle's relative velocity to the surrounding fluid [26]. In the current study, the particle Reynolds number is $Re_p = 18.8$, and Table 3.2 presents the obtained Reynolds numbers for the various models in this study.

Table 3.2: Fluid Reynolds numbers for the modeled flows.

	Reynolds numbers	
Model	$U_{in} = 1.5$ m s^{-1}	$U_{in} = 15$ m s^{-1}
M_1	1.00×10^5	1.00×10^6
M_2	1.00×10^5	1.00×10^6
M_3	1.50×10^5	1.50×10^6
M_4	1.00×10^5	1.00×10^6
M_5	1.50×10^5	1.50×10^6

3.3 Turbulence

Turbulent flows exhibit distinctive characteristics, including high disorder, irregularity, unsteadiness, complexity, and velocity fluctuations that evolve with time [24]. Such a flow is always dissipative due to the viscous shear stresses performing deformation work at the expense of kinetic energy. Another feature of turbulent flows is that they contain multi-scale vortices measured with different length scales, and the turbulent flow has a higher Reynolds number than a laminar flow. By calculating various parameters, it is possible to evaluate the turbulence level of a flow. These parameters include the turbulence intensity, the turbulent kinetic energy, and the dissipation rate, which can be calculated from Equation 3.12, Equation 3.13 and Equation 3.14, respectively.

$$I = 0.16Re^{-\frac{1}{8}} \tag{3.12}$$

$$k = \frac{3}{2}(I \cdot U)^2 \tag{3.13}$$

$$\omega = \frac{k^{0.5}}{C_{\mu}^{0.25}L} \tag{3.14}$$

C_{μ} is a constant equal to 0.09, and L is a reference length. The turbulence intensity, I, is a dimensionless parameter that is a ratio between the standard deviation of fluctuating velocity and the mean velocity of an internal flow [24]. These parameters have been calculated preliminary to the numerical simulations to enter as initialization parameters, and their values are presented in Table 3.3.

Table 3.3: Turbulence parameters used for initialization of the flows.

		$U_{in} = 1.5$ m s^{-1}		$U_{in} = 15$ m s^{-1}	
Parameter		M_1,M_2,M_4	M_3,M_5	M_1,M_2,M_4	M_3,M_5
I		3.80×10^{-2}	3.59×10^{-2}	2.84×10^{-2}	2.69×10^{-2}
k	[m^2 s^{-2}]	4.86×10^{-3}	4.34×10^{-3}	2.74×10^{-1}	2.44×10^{-1}
ω	[s^{-1}]	2.73×10^{1}	1.65×10^{1}	2.04×10^{-2}	1.24×10^{2}

3.4 Computational fluid dynamics

Computational Fluid Dynamics is a numerical analysis method to solve fluid flow problems [24]. The numerical software Ansys was employed to investigate the chosen problem for this study. The geometry was prepared in the CAD tool DesignModeler, the mesh was created using Ansys Meshing, and the simulations were performed using the solver Ansys Fluent. The post-processing was done by using CFD-Post and Ansys Fluent.

3.4.1 Turbulence model

The concerning models for the simulations performed are the RANS turbulence models. Looking at the features of the present case was essential in selecting a suitable turbulence model for this study. The case consists of an internal and external flow, meaning multiple boundary layers will exist. The $k-\omega\ SST-SAS$ model was selected due to its stability in boundary layer regions and ability to decrease turbulent flow fluctuations. It also accompanies a shear stress justification, presenting the turbulent kinetic energy from building near the stagnation points. Continuing, the turbulence models will be presented, followed by the governing equations.

The $k-\epsilon$ model is a two-equation linear eddy-viscosity turbulence model [27]. In addition to the equations for conservation, it solves two transport equations; one for the turbulent kinetic energy, k, and one for the turbulent kinetic energy dissipation rate, ϵ. The model is frequently used for free-shear layer flows with low-pressure gradients. The $k-\omega$ model is also a two-equation linear eddy-viscosity turbulence model [10]. This model solves for k, the turbulent kinetic energy, and ω, the specific turbulent dissipation rate. This model applies to flows with low Reynolds numbers, particularly when resolving the boundary layer's viscous sublayer region. This application is due to the $k-\omega$ model not including a damping function, such as the $k-\epsilon$ model, so the equations become simpler to solve near the walls.

It is established that $k-\epsilon$ is favorable in the free stream flow, while k-ω is favorable in boundary layer flows. The $k-\omega\ SST$ model combines the two models, making it a more stable turbulence model for a flow that includes both a boundary layer and a free stream. Here the $k-\epsilon$ model will be applied in the free stream regions of the flow, while the $k-\omega$ model will be applied in the inner layer of the boundary layer, such as the sublayer and logarithmic layer. Due to this shift of turbulence models and consideration of the shear stress in the boundary layer, the $k-\omega\ SST$ model provides a

better adverse pressure gradient than most of the other RANS turbulence models. A negative effect of employing the $k-\omega$ SST model is that it can create amplified turbulence levels in stagnation or acceleration regions compared to the regular $k-\epsilon$ model.

A further adjustment has been made to create the k-ω $SST-SAS$ model. It has been added a SAS-term, which intends to develop an increased value in the transient regions [28]. As ω increases, k and ν_T decrease, reducing fluctuations.

Governing equations

For the Navier-Stokes equations to be applicable in computational fluid dynamics, the equations must be discretized. Ansys fluent uses the finite-volume discretization method and stores the discrete values at the center of each cell [29]. The face values are interpolated from the cell center values and further used to solve the convection terms in the equations. Fluent offers multiple schemes to perform the interpolation, but for all simulations in this study, a second-order upwind scheme was applied, allowing for a higher-order accuracy.

The first equation given by the RANS equations is the continuity equation, which is presented in Equation 3.15. This equation is derived from the conservation of mass for a specified control volume and is valid for an incompressible flow [30].

$$\frac{\partial U_i}{\partial x_i} = 0 \tag{3.15}$$

U is here the flow mean velocity and for a 3D case the indices i and j are $i, j = 1, 2, 3$ and represent the directions of x, y and z. The Reynolds stress tensor, τ_{ij}, is presented in Equation 3.16. The stress tensor is derived from the fluctuating velocity u', which arises directly from an unsteady and turbulent flow [30]. It includes the turbulent kinetic energy k, the Kroenecker delta δ_{ij}, and the eddy viscosity ν_T.

$$\tau_{ij} = -\overline{u_i' u_j'} = -\frac{2}{3}k\delta_{ij} + \nu_T\left(\frac{U_i}{x_j} + \frac{U_j}{x_i}\right) \tag{3.16}$$

Further, the Reynolds-averaged momentum equation presented in Equation 3.17 includes a Reynolds stress tensor. Here, the equation's first term on the left-hand side denotes if the flow is steady or unsteady, where it for

this study is unsteady and varies with time. The term remains, as the flow is unsteady. The second term tells if the flow is 2D or 3D, which here is 3D. The first term on the right-hand side is a pressure term, the second is a viscous term, and the third is the Reynolds stress term.

$$\frac{\partial U_i}{\partial t} + U_j \frac{\partial U_i}{\partial x_j} = -\frac{1}{\rho}\frac{\partial p}{\partial x_i} + \nu \frac{\partial^2 U_i}{\partial x_j \partial x_j} - \frac{\partial \tau_{ij}}{\partial x_j} \tag{3.17}$$

The kinetic eddy-viscosity, ν_T, presented in Equation 3.18, is a scalar that describes the turbulent diffusion of mean momentum. In the $k-\epsilon$ model, this viscosity connects the kinetic energy with the energy dissipation.

$$\nu_T = \frac{C_\mu k^2}{\epsilon} \tag{3.18}$$

Equation 3.19 is the kinetic turbulence energy that the $k-\omega$ SST model solves, whereas Equation 3.20 is the dissipation rate that is solved [31].

$$\frac{\partial k}{\partial t} + U_j \frac{\partial k}{\partial x_j} = P_k - \beta^* k\omega + \frac{\partial}{\partial x_j}\left[(\nu + \sigma_k \nu_T)\frac{\partial k}{\partial x_j}\right] \tag{3.19}$$

$$\begin{aligned}\frac{\partial \omega}{\partial t} + U_j \frac{\partial \omega}{\partial x_j} = \alpha S^2 - \beta\omega^2 + \frac{\partial}{\partial x_j}\left[(\nu + \sigma_\omega \nu_T)\frac{\partial \omega}{\partial x_j}\right] \\ +2(1-F_1)\sigma_{\omega 2}\frac{1}{\omega}\frac{\partial k}{\partial x_i}\frac{\partial \omega}{\partial x_i}\end{aligned} \tag{3.20}$$

Here, P_k and P_ω are production terms, ν_T is the turbulent kinetic eddy viscosity for the $k-\omega$ SST model, σ_k and σ_ω are the turbulent Prandtl numbers for the kinetic energy and the dissipation rate, respectively. F_1 is a blending function that the $k-\omega$ SST model utilizes to combine the $k-\epsilon$ and $k-\omega$ models [31]. The kinematic eddy viscosity for the $k-\omega$ SST model, given in Equation 3.21, differs from the $k-\epsilon$ model due to it also including the strain rate magnitude, $\mathbf{S}$.

$$\nu_T = \frac{a_1 k}{max(a_1\omega, F_2\mathbf{S})} \tag{3.21}$$

In this equation, a_1 is a constant, and F_2 is a function that varies with the flow. F_1 will equal one for boundary-layer flows and zero for free shear

flows [10]. The SAS term in Equation 3.22 reduces the velocity fluctuation sensitivity of the dissipation.

$$P_{SAS} = \tilde{\zeta}_2 \kappa S^2 \frac{L}{L_{vK,3D}}, \;\; L_{vk,3D} = k \frac{S}{U''} \tag{3.22}$$

In the SAS term, S is the first velocity gradient, and U'' is the second velocity gradient for the flow. $L_{vK,3D}$ is the von Kármán length scale for the instantaneous velocities, which is a 3D formulation of the von Kármán length scale in 1D, $L_{vK,1D}$. The SAS term is a production term and is added to the $k-\omega$ SST model, as presented in Equation 3.23,

$$\begin{aligned} \frac{\partial \omega}{\partial t} + U_j \frac{\partial \omega}{\partial x_j} = P_\omega - \beta \omega^2 + \frac{\partial}{\partial x_j}\left[(\nu + \sigma_\omega \nu_T)\frac{\partial \omega}{\partial x_j}\right] \\ +2(1-F_1)\sigma_{\omega 2}\frac{1}{\omega}\frac{\partial k}{\partial x_i}\frac{\partial \omega}{\partial x_i} + P_{SAS} \end{aligned} \tag{3.23}$$

where β is a constant [31]. The new production term, P_{SAS}, will increase as the von Kármán length decreases, leading to a steadier flow in regions with finer mesh as the flow becomes more turbulent. This can be seen in Equation 3.23 by observing that an increase in P_{SAS} leads to a decrease in the turbulent kinetic energy and the eddy viscosity.

3.4.2 Multiphase flow

The flow to be considered in this study is a multiphase flow, consisting of two distinct phases, decided to be water and sand particles. Water serves as the continuous and primary fluid phase, while sand particles exist in a solid state, resulting in an inherently heterogeneous flow.

DPM is applied to solve the transport of one phase through another in CFD. This model follows the Euler-Lagrange approach, where the fluid phase gets solved through the Navier-Stokes equations and the particles get solved by tracking them in the fluid [32]. The limitation of the DPM is the assumption that the volume fraction of the solid phase is lower than the fluid phase [33]. This study contains numerical simulations with a small particle-to-fluid ratio, hence the DPM will be sufficient for this work. Table 3.4 shows the particle-to-water volume ratios, and it can be seen that the volume fraction of the particles is less than 10%. Therefore the DPM is considered to be sufficient enough [32].

Table 3.4: Volume fractions of particles in the particle-laden flows.

	Volume fractions	
Model	$U_{in} = 1.5$ m s^{-1}	$U_{in} = 15$ m s^{-1}
M_1	7.34×10^{-8}	7.34×10^{-9}
M_2	7.36×10^{-8}	7.36×10^{-9}
M_3	7.44×10^{-7}	3.35×10^{-9}
M_4	7.36×10^{-8}	7.36×10^{-9}
M_5	7.44×10^{-7}	3.35×10^{-9}

When simulating a multiphase flow, it is possible to investigate how the phases within the domain interact. Ansys Fluent allows for two multiphase solvers within the DPM solver, a one-way coupled and a fully-coupled model. The one-way coupled model uses DPM to solve how one phase interacts with the other, considering only the continuous fluid effects on the particles. The fully-coupled model considers the interactions between the fluid and the particles and their effects on each other. Ansys Fluent uses an empirical model for the particle-fluid interaction for the sub-grid particles. In contrast, the particles are treated as point masses in the solver for the particle-particle interactions [26]. One-way coupling is insufficient if the particles affect the flow or particle-particle interactions are present. The Stokes numbers for this study, provided in Table 3.1, indicate strong coupling between the particles and the flow. Given the potential for particle interactions due to mixing and aggregation, using a fully-coupled solver is essential, despite the increased computational cost.

A flow through a real sand trap will consist of three phases: water, sand, and air. The reduction to a two-phase flow causes the momentum exchange between the water and air, and the particle and air, to be neglected. The simplification is made because the computational costs are greater for three-phase simulations, compared to two-phase simulations, in addition to the time restriction of the study.

3.4.3 Mesh

For Ansys to discretize a domain, the domain must first be divided into several elements, commonly referred to as a mesh. It is essential to develop a high-quality mesh to get a high simulation accuracy [34]. Therefore, striving towards achieving the best mesh possible for the domain is necessary. In addition to getting higher calculation accuracy, a higher quality mesh causes

the numerical simulations to improve concerning calculation time and convergence. A finer mesh gives a more accurate solution at a higher computational cost, whereas a coarser mesh gives a less accurate solution at a lower computational cost. Because of these factors, evaluating the computational capacity available and finding a suitable balance between a coarse and fine mesh becomes necessary. When the mesh is ready for simulations, Ansys Fluent applies Finite Volume Equations to all the elements. As these are applied and calculated for each element, they represent the entire domain's flow behavior.

To have a sufficient mesh, it is essential to obtain the correct values for different quality parameters. The selection of appropriate quality parameters for the mesh depends on the specific characteristics and requirements of the studied domain. In this study, the domain was to be meshed as a structural mesh with hexahedrons. The contents and criteria for specific quality parameters are described in Table 3.5. In this study, a mesh was considered of sufficient quality if it met the criteria, and satisfactory values were achieved for both the orthogonality, skewness, and element quality.

Table 3.5: Description of mesh quality parameters.

Parameter	Description
Orthogonality	How close the angles between the element faces are. For a structural hexahedral mesh the optimal angle is 90°. It is measured in a value of $0<\gamma<1$, where 1 is the highest quality and 0 is the lowest quality.
Skewness	Indicates the asymmetry of the element compared to an ideal element. It is measured in a value of $0<\gamma<1$, where 0 is the ideal cell and highest quality.
Element	Indicates an overall quality for the mesh. It is measured in a value of $0<\gamma<1$, where 1 is the best quality, and 0 is the lowest.

The requirements gathered in Table 3.5 are guidelines developed by Ansys on the quality parameter value [35]. A GCI study was conducted to review the mesh resolution and its independence, and the procedure and results are presented in Chapter 3.6.

3.4.4 y^+ value

Ensuring an adequate quality of the boundary layers near the walls and obstructions requires evaluation of the size and placement of the cells. This evaluation determines the y^+ value, a non-dimensional distance parameter that depends on the fluid velocity [24]. It provides insights into the appropriate cell size and resolution for accurately capturing the flow behavior in these regions. The appropriate y^+ value needed for resolving the boundary layer in a turbulent flow depends on the turbulence model employed for solving the equations and the specific geometry of the domain under study. It is important to carefully consider these factors to ensure accurate and reliable results in capturing the turbulence characteristics near the boundary. The $k-\omega\ SST-SAS$ is, in the current study, applicable throughout the boundary layer and free stream regions. For the boundary layers' viscous sub-layer to be solved correctly, the desired value should be $y^+ < 1$, while for the buffer layer, it should be $5 < y^+ < 30$ [36].

The transition from smaller elements in the near-wall regions to larger elements further out in the boundary layer was achieved by employing a bias function on the vertices during the element creation process. A manual method was chosen over automatic inflation layers due to the limited adaptability of the structured mesh. Having smaller elements close to the walls lead to a smaller y^+ value in this region, giving a more accurate calculation when resolving the boundary layer and capturing the flow separation. Since the study focuses on investigating the flow downstream of the cylinder, having larger cells near the inlet and outlet was considered acceptable. It is also important to keep the transition regions between the fine and coarser regions of the mesh smooth to get an accurate solution. An abrupt transition leads to accurate calculations in some areas and less accurate in others, causing undesired irregularities.

Table 3.6: Mesh specifics towards the bounded surfaces of the domain and y^+ values for GCI_{medium}.

Parameter	Value
Inner layer size, cylinder	7.0×10^{-6} m
Outer layer size, cylinder	6.0×10^{-5} m
Number of layers, cylinder	10
Inner layer size, top/bottom wall	7.5×10^{-5} m
Max $y^+_{cylinder}$	2.4×10^{0}
Max y^+_{walls}	1.3×10^{1}

Table 3.6 displays the y^+ values obtained for this study. The presented values regard the top-and-bottom walls and the cylinder walls, all subject to a no-slip boundary condition. The y^+ values are lower for the cylinder walls than for the top-and-bottom walls, which is coherent with a smaller inner layer size for the cylinder walls than the tunnel walls. Based on the recommended y^+ values, the values presented in 3.6 are deemed sufficient for this study. The values were acquired from the simulation of GCI_{medium} in the GCI study, which involved a particle-laden steady flow to closely resemble the case for the numerical simulations to be conducted.

3.5 Simulation models

This chapter introduces the models used for the present study. As mentioned, the models created are simplified models of a pressurized sand trap design. Model 1, the base model for the other models, is illustrated from an isometric perspective in Figure 3.2. The model consists of a rectangular tunnel with ribs upstream of the outlet, and the cross-sectional tunnel area is given in Table 2.2. Measurements and specifics are illustrated in the mechanical drawings of the models in Appendix B.

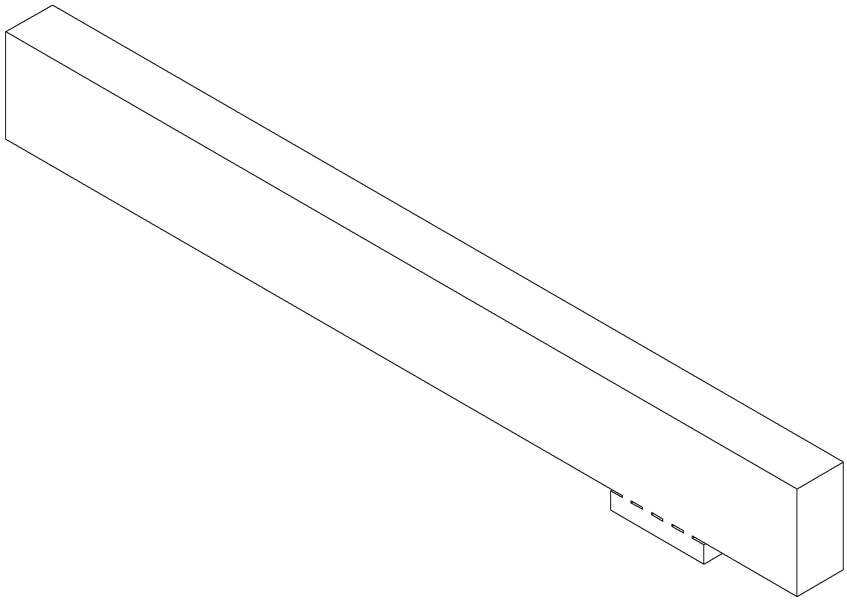

Figure 3.2: Model 1: tunnel with ribs.

A closer look at the ribs is illustrated in Figure 3.3. The ribs are incorporated to investigate whether the settled particles will be trapped or re-suspended towards the tunnel outlet. The rib section comprises five identical horizontal plates positioned at the tunnel bed.

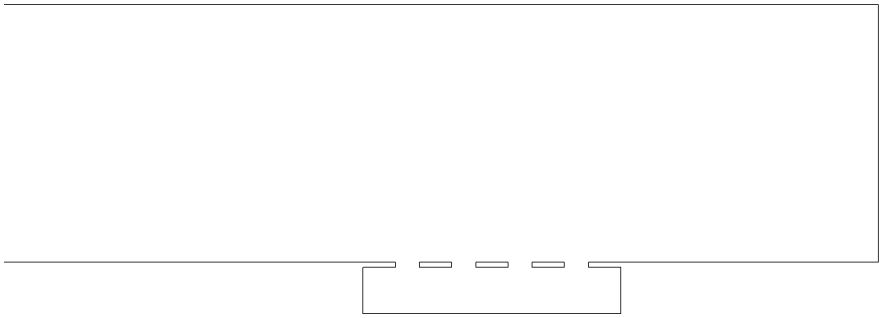

Figure 3.3: Close-up view of the rib section.

Figure 3.4 shows the FCS used in models 2 and 4, seen from the top of the tunnel. Model 2, shown in Figure 3.4(a), can be seen to have a single square cylinder, representing the FCS, while Model 4, shown in Figure 3.4(b), has a single circular cylinder. Both these cylinders are vertically placed at $x = 0.145$ m downstream of the tunnel inlet.

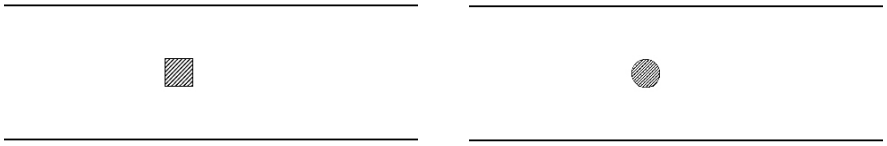

(a) Model 2: Single square FCS.

(b) Model 4: Single circular FCS.

Figure 3.4: Simulation models consisting of a single FCS.

Furthermore, additional models were created incorporating multiple cylinders, as illustrated in Figure 3.5. Model 3, illustrated in Figure 3.5(a), consists of three vertically arranged square cylinders positioned at $x = 0.145$ m downstream of the tunnel inlet. In Model 5, shown in Figure 3.5(b), three circular cylinders are located at the same distance from the inlet.

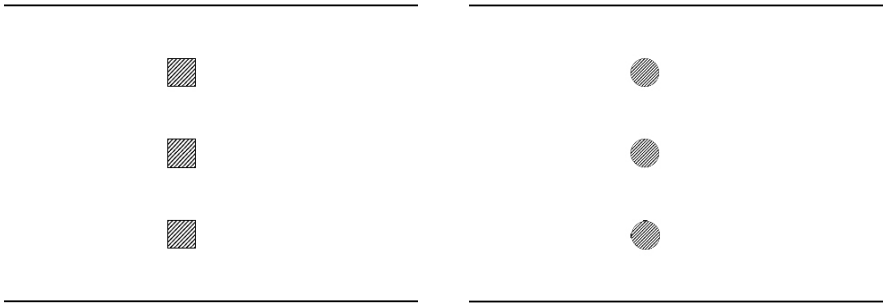

(a) Model 3: Three square FCS. **(b)** Model 5: Three circular FCS.

Figure 3.5: Simulation models consisting of multiple FCS.

Multiple FCS variations were tested to observe the particle behavior under the influence of a single vortex street and, subsequently, to investigate how the influence from other vortices affects it. The various geometries have been made to see if there is a sufficient difference in the generated turbulence between them and how this potential difference will influence the particles. These named differences will help better understand how the two-phase flow behaves and how the particle settlement is affected.

3.6 Mesh independence study

A grid convergence index study is crucial to validate the mesh before conducting simulations. Such an analysis enables assessing the impact of mesh density and quality on the results [37]. This method ensures that the simulations have a minimized discretization error of the domain while still having the accuracy needed. The desired outcome of a GCI study is that the discretization error asymptotically approaches zero, indicating that the numerical analysis provides a realistic result independent of the mesh [37]. Achieving the desired outcome entails refining the mesh and determining the optimal level of refinement. The result of the GCI study is a value, a discretization error, involving the quantification of the discrepancy between the computed value and the asymptotic numerical value. The method presented by Celik et al. [38] was applied in this study.

Table 3.7: Quality parameters and their values for the refined meshes in the GCI study.

Parameter	GCI_{fine}	GCI_{medium}	GCI_{coarse}
Orthogonal quality	0.998	0.998	0.997
Skewness ratio	0.004	0.005	0.006
Element quality	0.345	0.338	0.379

Three meshes with varying degrees of refinement were generated to perform the GCI analysis, sharing the same structure but differing in their level of detail. Examining the quality parameters, presented in Table 3.7, is a method to confirm that the meshes have identical characteristics. All three cases have approximately the same qualities for orthogonality, skewness, and element quality, indicating that they have the same features. The mesh refinement models are GCI_{fine}, GCI_{medium} and GCI_{coarse}, containing N_1, N_2 and N_3 elements, respectively. The mesh resolutions are shown in Figure 3.6, where the difference in the number of elements can be observed.

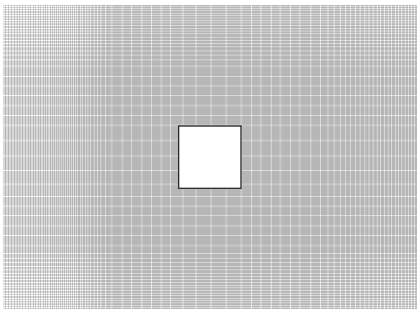

(a) GCI_{fine} containing N_1=4.26×10^7 elements.

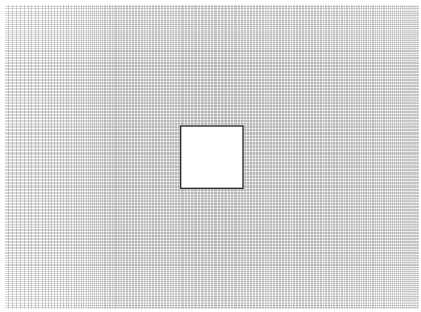

(b) GCI_{medium} containing N_2=1.67×10^7 elements.

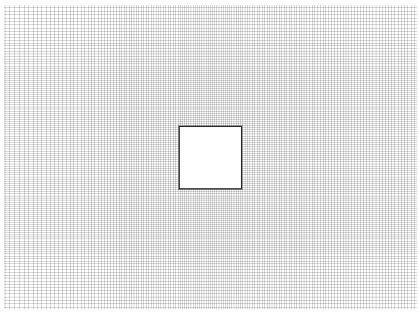

(c) GCI_{coarse} containing N_3=6.83×10^6 elements.

Figure 3.6: The refined meshes employed in the GCI analysis.

One simulation for each mesh was necessary to perform the GCI study. The numerical simulations were all steady simulations with one-way coupled particle injection through DPM in Ansys Fluent, and the setup employed is shown in Table A.1 in Appendix A. They were all initialized and run to a steady and stable state before the particle injection. The GCI simulations resemble the forthcoming simulations, differing by being steady and one-way coupled.

Table 3.8 presents the parameters extracted and calculated from the GCI study. The refinement factors, denoted as r_{21} and r_{32}, are calculated from the mesh size and are factors to quantify the level of refinement between different mesh resolutions [38]. The parameters ϕ_1, ϕ_2, and ϕ_3 correspond to simulation outcomes, specifically the total pressure head loss over the cylinder within the tunnel. The total pressure head loss comprises frictional losses and local pressure head losses resulting from viscosity and variations

Table 3.8: The extracted and calculated parameters in the GCI study and the results for the discretization error and asymptotic value.

Parameters	Value
N_1, N_2, N_3	4.26×10^7, 1.67×10^7, 6.83×10^6
r_{21}	1.37
r_{32}	1.35
ϕ_1	1.00×10^3
ϕ_2	9.93×10^2
ϕ_3	9.83×10^2
p	1.83
ϕ_{ext}^{21}	1.00×10^3
e_a^{21}	0.63%
e_{ext}^{21}	0.80%
GCI^{21}	1.01%
GCI^{32}	1.84%
$GCI_{asymptotic}$	1.01

in geometry. However, in this study, the local pressure head losses are neglected due to the constant cross-section of the tunnel. The pressure is measured at two cross-sectional planes at $x_1 = 0.1$ m upstream and $x_2 = 0.3$ m downstream of the cylinder, shown in Figure 3.7.

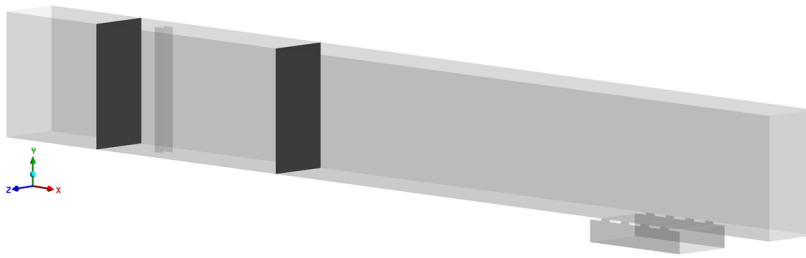

Figure 3.7: The representative planes at which the total pressure was measured for the GCI calculations.

Equation 3.24 was used to calculate the pressure head loss,

$$\Delta h_L = \frac{p_1 - p_2}{\rho g} \tag{3.24}$$

where p_1 and p_2 are the total pressures at the respective planes. A second-order scheme has been used for the simulations, meaning that the order of convergence, p, should be approximately 2. From Table 3.8 it is observed that the simulations result in an order of convergence of $p = 1.83$, which is in an acceptable range of 2. $GCI_{asymptotic}$ indicates the asymptotic range of convergence and is a parameter that, when it is approximately 1, suggests that the solutions are within the asymptotic range of convergence [37]. If the value is not close to 1, the results are not asymptotically approaching a converged solution, meaning the numerical simulation results are not mesh-independent. The value is here 1.01, validating the results contained in the GCI study.

The results from the GCI study indicated that using the model and mesh from GCI_{medium} is sufficient when proceeding forward. Due to constraints in time and computational resources, the GCI study was conducted for one out of the five models. Since the models have resembling features, the structure for GCI_{medium} was used when discretizing the remaining models.

3.7 Simulation setup and physics

All the models are simulated with a flow inlet velocity of U_{in}=1.5 m s^{-1}. Additionally, Model 1 and Model 2 are simulated with an inlet velocity of U_{in} = 15 m s^{-1}. Table 3.9 and Table 3.10 provide the setup and solution parameters for the simulations with U_{in} = 1.5 m s^{-1} and U_{in} = 15 m s^{-1}, respectively, utilized in Ansys Fluent. These particular inlet velocities were decided to uphold the turbulence levels decided from the Reynolds numbers for the study, presented in Table 3.2. By running two cases that cause different turbulence levels, it will be possible to compare how the cylinders, velocity, and turbulence affect the behavior of the particles. All the simulations were initialized with an unsteady and stable flow, reducing the particle injection time. Due to the tunnel's length of 0.85 m, it takes approximately t = 0.567 s for the water and particles to pass through the tunnel at the inlet velocity of U_{in} = 1.5 m s^{-1}. Similarly, at the higher inlet velocity of U_{in} = 15 m s^{-1}, the passage time reduces to approximately t = 0.0567 s. Therefore the discrete phase, containing particles, was chosen to have an injection time of t = 1.9 s and t = 0.12 s.

The optimal time step size for the given inlet velocity of U_{in} = 1.5 m s^{-1} was determined to be Δt = 0.005 for the square cylinder and Δt = 0.002 for the circular cylinder. The numerical simulations successfully captured the underlying flow physics by employing these specific time step sizes and conducting ten iterations per time step. The variation in time step sizes is attributed to the cylinder geometries and vortex shedding frequency. Blunt objects induce vortex shedding at a lower frequency than less blunt objects, meaning the square cylinder has a lower shedding frequency, allowing for a larger time step size. For the flows with an inlet velocity of U_{in} = 15 m s^{-1}, the time step size became Δt = 0.00005 for the square cylinder, also here with ten iterations per time step.

Particle-laden flow simulations were conducted for both inlet velocities in Model 1 and the lower inlet velocity in Model 2 and Model 4. These specific cases were chosen as they adequately showcase the flow characteristics and behavior, providing sufficient understanding and evaluation of the particle behavior to assess the remaining models simulated only as single-phase flows.

The boundary conditions for the top-and-bottom walls are the no-slip condition since the walls are rigid and stationary while the fluid flows past. Therefore, it is an appropriate assumption that the flow velocity against these walls is the same as the velocity of the walls, which is zero. In the tunnel, the side walls are considered to have free-surface flow boundary con-

Table 3.9: Simulation and solution setup for $U_{in} = 1.5$ m s^{-1} in Ansys Fluent.

Parameter	Description	Setting
General	Transient	
	Gravity[1]	$g = 9.81$ m s^{-2}
Turbulence model	k-ω SST-SAS	
Materials	Solid particles	$\rho_p = 1.600 \times 10^3$ kg m^{-3}
	Incompressible fluid	$\rho = 9.982 \times 10^2$ kg m^{-3}
		$\nu = 1.003 \times 10^{-6}$ m^2 s^{-1}
Discrete phase	Two-way coupled	
	Particle diameter	$D = 0.0002$ m
	Injection interval	$t = [4.1, 6]$ s
Boundary conditions	Inlet	$U = 1.5$ m s^{-1}
	Cylinder walls	No-slip
	Top and bottom wall	No-slip
	Side walls	Free-shear
Method	Scheme	Coupled
	Pressure	Second order upwind
	Momentum	Bounded central differencing
	Turbulent kinetic energy	Second order
	Specific dissipation rate	Second order
	Transient formulation	Bounded second order implicit
Calculation	Total time	6 s
	Time step size	Square cylinder: 0.005 s
		Circular cylinder: 0.002 s
	Iterations	10

[1] The particle-laden simulations for Model 1 and Model 4 included gravity, while it was neglected for Model 2.

ditions, implying that the flow experiences zero parallel shear stress and zero perpendicular normal stress. This decision was based upon the flow not having any interference from the walls so that the case with one cylinder can be compared with the case of three cylinders. The flow is initiated by setting an inlet flow velocity, leading the inlet-and outlet pressure to be set by the flow. Applying the inlet velocity prevents setting incorrect pressure values, which causes the simulation to diverge.

All the simulations were conducted with a coupled algorithm using a pressure-based solver that calculates the momentum and continuity equations together [39]. In this solver, the pressure equation is derived from the continuity and momentum equations, ensuring that the velocity field satis-

Table 3.10: Simulation and solution setup for $U_{in} = 15$ m s^{-1} in Ansys Fluent.

Parameter	Description	Setting
General	Transient	
	Gravity	$g = 9.81$ m s^{-2}
Turbulence model	k-ω SST-SAS	
Materials	Solid particles	$\rho_p = 1.600 \times 10^3$ kg m^{-3}
	Incompressible fluid	$\rho = 9.982 \times 10^2$ kg m^{-3}
		$\nu = 1.003 \times 10^{-6}$ m^2 s^{-1}
Discrete phase	Two-way coupled	
	Particle diameter	$D = 0.0002$ m
	Injection interval	$t = [0.07, 0.19]$ s
Boundary conditions	Inlet	$U = 15$ m s^{-1}
	Cylinder walls	No-slip
	Top and bottom wall	No-slip
	Side walls	Free-shear
Method	Scheme	Coupled
	Pressure	Second order upwind
	Momentum	Bounded central differencing
	Turbulent kinetic energy	Second order
	Specific dissipation rate	Second order
	Transient formulation	Bounded second order implicit
Calculation	Total time	0.19 s
	Time step size	Square cylinder: 0.00005 s
	Iterations	10

fies the continuity equation. The coupled solver stores the discrete system of all the momentum and continuity equations while solving for the velocity and pressure fields. This method requires more computational memory than the non-coupled algorithms. However, to compensate, it provides a better and more accurate solution convergence rate for transient simulations than other solver algorithms.

Chapter 4

Results and discussions

This chapter presents and discusses the results within the study's scope. The numerical simulations conducted are provided in Table 4.1, and each model will be individually presented before an overall discussion regarding particles in a sand trap at the end of the chapter. The simulations with an inlet velocity of $U_{in} = 1.5$ m s^{-1} and $U_{in} = 15$ m s^{-1} will hereafter be referred to as the standard and elevated flow case, respectively. The selection of different cylinders to represent sand trap FCS aims to determine which geometry yields more favorable particle behavior. The investigation to determine the more advantageous shape for an FCS stems from the shapes generating distinct vortices, necessitating further analysis. Flow factors of interest are the flow turbulence levels, turbulence energy, and velocity. The study has focused on examining the flow characteristics, explicitly focusing on flow patterns and interactions between vortices. The results will be analyzed regarding flow and particle characteristics, and their correlation with the underlying principles of a hydropower sand trap will be explored. To comprehend particles' behavior, the study has investigated how particle trajectories compare to the flow streamlines, observing whether the particles behave independently of the flow. Additionally, the study will investigate whether the particles form clusters or remain dispersed.

Table 4.1: The simulations conducted in this study.

Model	Simulations			
	$U_{in} = 1.5$ m s^{-1}		$U_{in} = 15$ m s^{-1}	
	Single-phase	Multiphase	Single-phase	Multiphase
M_1: Ribs	✓	✓	✓	✓
M_2: Single square cylinder and ribs	✓	✓	✓	
M_3: Multiple square cylinders and ribs	✓			
M_4: Single circular cylinder and ribs	✓	✓		
M_5: Multiple circular cylinders and ribs	✓			

4.1 Presentation method for the results

The flow results are presented as contour plots, visualizing the data on different planes. The planes used for presentation are the ZX-plane and the XY-plane, illustrated in Figure 4.1 and Figure 4.2, respectively. The selected planes represent the flow characteristics least affected by the boundary conditions of the surrounding surfaces.

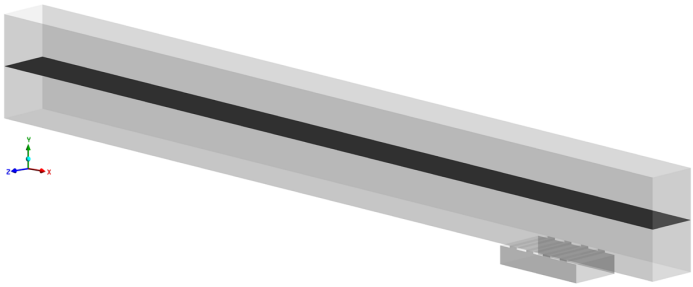

Figure 4.1: ZX-plane through the centerline of the tunnel.

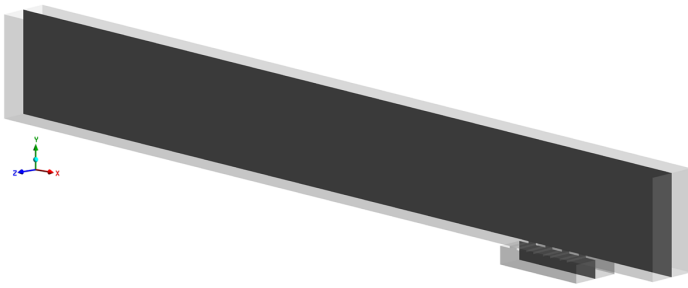

Figure 4.2: XY-plane through the centerline of the tunnel.

Additionally, the flow results are presented on the plane of the tunnel outlet to visualize the flow's asymmetry and symmetry across the tunnel's cross-section. Providing such results gives a more comprehensive understanding of the flow behavior in a three-dimensional scenario, which is vital in a complex flow such as here. The particle injections' results and behavior are presented as figures from specific times of the flow, consisting of the entirety of the channel. These times match the times of the single-phase flow, getting a more comprehensive picture of how the particles and water interact compared to the water itself.

4.2 Model 1

The base case, consisting of Model 1, was created to determine how the water flow and particles generally behave in a sand trap without an upgraded design. Observing the flow pattern and behavior, especially along the surfaces and past the ribs, is relevant concerning particle settlement. It is also necessary to investigate the flow behavior before the particle injection to determine how the particles' mass load and potential accumulation affect the flow.

4.2.1 Standard flow case for Model 1

Single-phase flow with water

Figure 4.3 shows the contour plots of the total velocity at the respective planes for the standard velocity unladen flow. The total velocity includes the velocity magnitude in the x,y, and z directions, describing the 3D effects more entirely. The velocity downstream of the inlet is shown in the upper plot of Figure 4.3(a), which corresponds to the plane illustrated in Figure 4.1, while the bottom figure represents the velocity on the plane shown in Figure 4.2. The center velocity slightly increases throughout the tunnel, which is observed by the color being more potent at the tunnel outlet than at the inlet. The color differences also make it visible that the velocity remains constant in the cross-sectional direction while it encounters velocity differences between the top and bottom surfaces.

The velocity increase along the center originates from the flow development through the tunnel. While the flow has reached a stable condition, it should be noted that it has yet to fully develop due to the limited time and distance available in the tunnel. As the flow encounters the transition to become a fully developed turbulent flow, the velocity is influenced by the boundary conditions of the walls. The tunnel's side walls have a zero-shear condition, with no velocity gradient along them. As depicted in Figure 4.3(a), it is evident that the velocity decreases progressively along the top and bottom surfaces downstream, forming a boundary layer. This velocity variation results from the no-slip condition, ensuring that the fluid in contact with the stationary wall adopts the same velocity as the wall. The flow behavior resulting from these boundary conditions is twofold. Firstly, certain regions of the tunnel flow, such as the boundary layer, experience a velocity deceleration. Secondly, the free stream region of the tunnel, such as the centerline, exhibits a velocity acceleration. These flow effects demon-

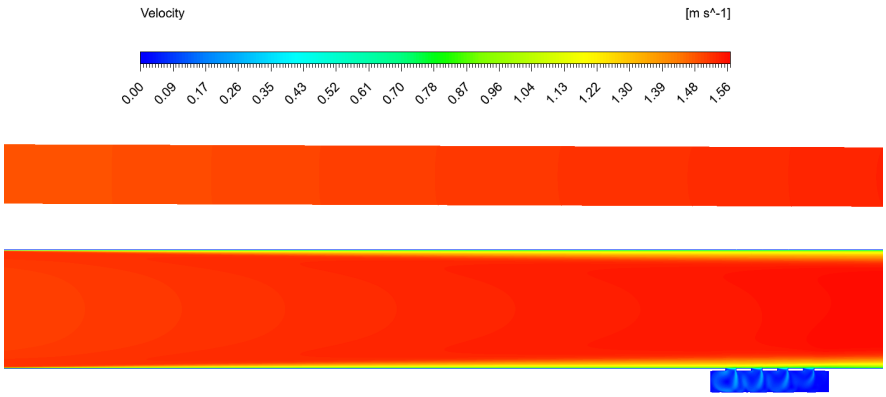

(a) Velocity contours at the respective planes.

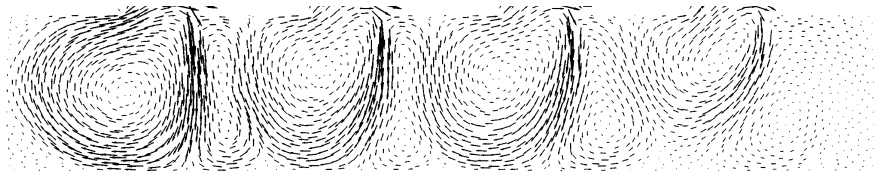

(b) Velocity vectors visualizing flow trajectories in the rib section.

Figure 4.3: Velocity contours and trajectories of the standard flow for Model 1.

strate the boundary conditions' influence on the tunnel's velocity distribution. Although the RANS turbulence model used for the numerical simulations presupposes that the flow is fully developed and turbulent, the added SAS term stabilizes the flow fluctuations of the non-fulfilled prerequisite. To account for the non-developed flow, it would be necessary to have an LES or DNS, which comes at a higher computational cost.

Based on the velocity information provided in Figure 4.3(a), it can be observed that there is a significant velocity reduction within the rib section. Several factors contribute to this decrease. Firstly, as the flow separates, there is an abrupt expansion in the flow area. According to the principle of continuity, which ensures the conservation of mass flow rate, this volume expansion necessitates a corresponding velocity decrease. Secondly, the rib section features a no-slip boundary condition, which further contributes to the velocity reduction.

Figure 4.3(b) illustrates the flow trajectories within the rib section. The separation in the rib section beneath the boundary layer leads the flow to encounter a backflow upon entrance, generating recirculation regions. The recirculation occurs due to low-pressure zones generated beneath the ribs, attracting the flow towards them. Figure 4.4(b) shows the pressure drop beneath the ribs, leading to the creation of recirculation. By comparing the velocity from Figure 4.3(b) and the pressure from Figure 4.4(b), it is observed that the recirculation regions decay for the ribs further downstream. The first rib opening experiences the most significant pressure drop, while the last opening encounters the least significant pressure drop, resulting in decreasing recirculation regions along the rib section.

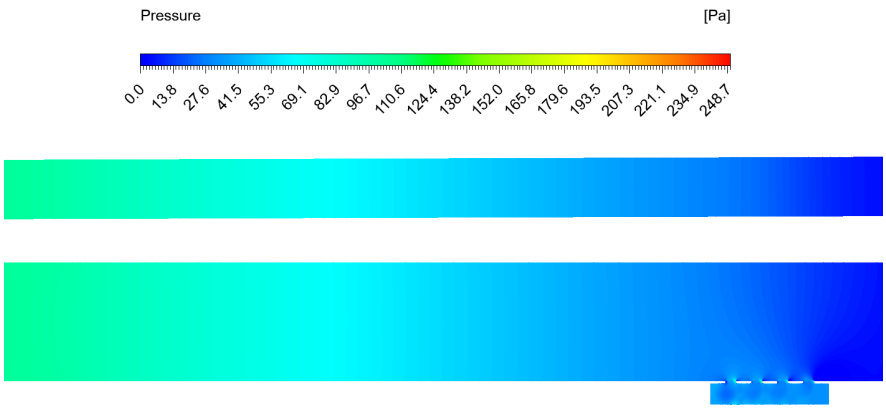

(a) Pressure at the respective planes.

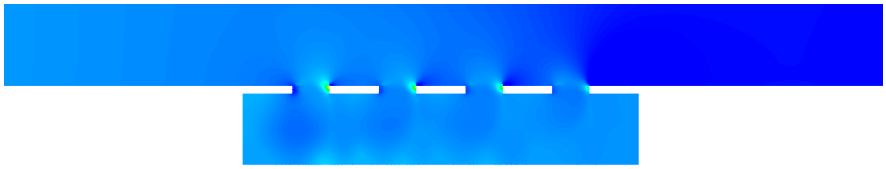

(b) Pressure in the rib section.

Figure 4.4: Pressure contour of the standard flow for Model 1.

The pressure distribution of the flow through the tunnel is depicted in Figure 4.4(a). The smooth color transition observed between the tunnel inlet and outlet confirms the absence of abrupt disturbances within the tunnel, except for the regions where the ribs are located. The smooth pressure

decrease is desirable, allowing for minimized turbulence and dissipative losses throughout the tunnel.

The flow's turbulent kinetic energy is plotted in Figure 4.5, where the upper plot of Figure 4.5(a) shows that the energy decreases along the tunnel center. The bottom plot shows that the energy decrease originates from increased energy along the tunnel surfaces containing no-slip boundary conditions. Deceleration of the flow at the no-slip surfaces results in momentum transfer between the mean flow and fluctuating velocity components, as well as viscous forces. These factors amplify shear stresses, elevating the TKE along these surfaces.

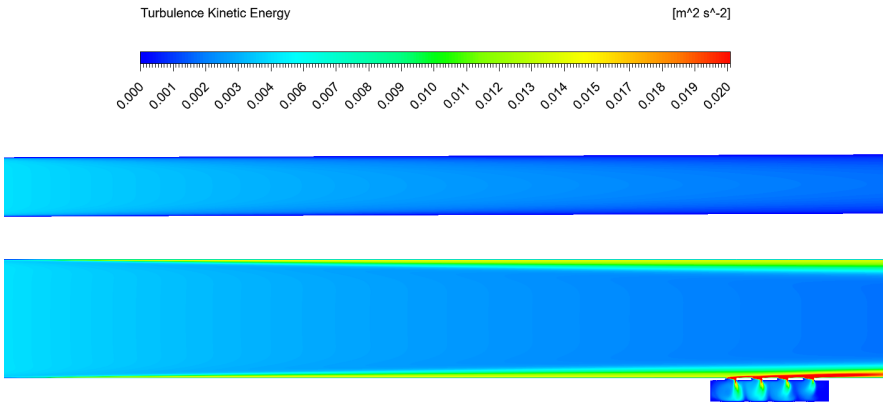

(a) TKE at the respective planes.

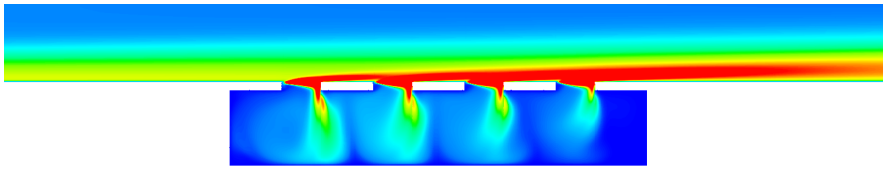

(b) TKE in the rib section.

Figure 4.5: TKE contour of the standard flow for Model 1.

Moreover, it is notable from Figure 4.5(b) that the flow separation upon entering the rib section causes enhanced energy. The flow undergoes various velocities during separation, amplifying shear stresses and energy, leading to a more complex flow. Additionally, the recirculation causes the flow to mix

as it reattaches, generating more turbulence.

Multiphase flow with water and particles

The particle-laden simulations were conducted with two-way coupling between the water and the particles to examine all the interactions present. There was no significant difference in this model's flow properties from the single-phase flow to the particle-laden flow. The flow behaves approximately the same, resulting in the number of particles and their size being non-influential to the flow. The Stokes number implied that the particles would not influence the water, which proved correct.

Particles were injected across the entire inlet area of Model 1 with velocities equal to the flow inlet velocity to disperse suspended particles in the flow. Figure 4.6 shows the particles and their velocity in the tunnel at $t = 1.9$ s after injection start. It is observed that the particles exhibit a uniform and dispersed pattern through the tunnel, with no irregularities or deviations. Such particle behavior occurs due to a relatively high flow velocity, a small particle size, and a low particle volume, which will be further elaborated.

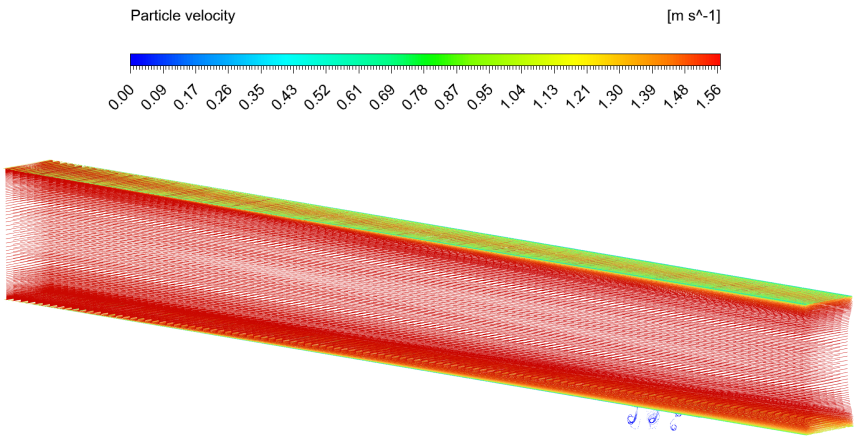

Figure 4.6: Particles and their velocity from the standard flow for Model 1.

From Figure 4.7(a), it becomes visible that there is a higher particle density near the tunnel's top and bottom surfaces. The gathering of particles along these boundaries corresponds to the deceleration of velocity in these regions, as evidenced by the velocity specter for the particles. As can be

seen, the particles are coupled with the flow, meaning a flow velocity reduction gives a particle velocity reduction. Due to the flow having a high inlet velocity, the velocity gradients along the no-slip surfaces exhibit steep characteristics. A steeper velocity gradient minimizes the particles' probability of entering through the ribs due to the high velocity counteracting the suction from the low-pressure zones beneath the ribs. In the case of a less steep velocity gradient, there would have been a higher probability of particles having a stronger attraction toward the low-pressure zones beneath the ribs. Most particles in the current case exhibit enough strength to withstand this attraction, hence resisting entering the rib section. Depending on the flow velocity through a sand trap in a hydropower plant, adjusting the space between the ribs would be beneficial, allowing particles to have an appropriate timespan to enter.

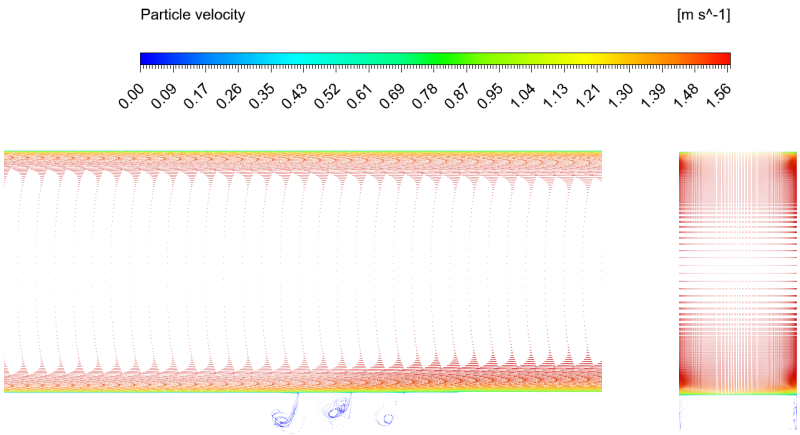

(a) Side view. **(b)** Outlet view.

Figure 4.7: Particles and their velocity from a side view and outlet view from the standard flow for Model 1.

In addition to the stationary surfaces playing a part in the near-wall accumulation of particles, the inertial forces of the flow also contribute. The current flow exhibits a high Reynolds number, indicating that the inertial forces dominate over viscous forces. These inertial forces contribute by forcing the particles out of the center streamline and towards the surrounding boundaries of the tunnel, which can be observed from Figure 4.7(b). Due to the particles being forced towards the tunnel corners, the particles primarily

enter the rib section from the tunnel's side surfaces. Figure 4.7(a) reveals that apart from the particles gathering to the upper and lower surfaces with similar velocities, there is only a marginal variation in the particle density between the two surfaces. It is also present that only the particles caught in the rib section obtain a zero velocity, resulting in none of the particles in the tunnel settling. These results indicate that the velocity, and hence the inertial forces, are forceful and impede the settlement of particles suspended in the flow.

Despite the evident relocation of particles towards the top and bottom surfaces, several factors contribute to the absence of particle clustering. A contributing factor to the hindrance of particle clustering is the presence of high inertial forces, which disrupt particle-particle interactions. This disruption occurs because the particle trajectories remain aligned in the streamwise direction, preventing particle interactions. Consequently, while the particles are brought closer to each other, they continue to remain dispersed rather than forming clusters. A second reason for the particles not clustering is their size and low volume ratio, further contributing by minimizing the probability of particle interactions.

The particle results corroborate the findings of Maxey and Corrsin [3], who noted that the particles were not indefinitely suspended due to the influence of inertial forces. The inertial forces on the particles contribute to their eventual settling and non-permanent suspension within the flow by initating them to accumulate towards the surfaces. The results also agree with the findings of Nielsen [4] due to the strong turbulence increasing the particle settling velocity. Therefore, the simultaneous presence of high velocity and inertial forces is unfavorable for particle settlement, necessitating the discovery of an optimal balance between the two factors to attain the most effective particle settlement conditions. It would also be essential to obtain a realistic inlet velocity for the sand trap to design the ribs with suitable spacing.

4.2.2 Elevated flow case for Model 1

A comparative case was conducted with a higher inlet velocity, resulting in a higher Reynolds number flow. This higher velocity flow was specifically performed to facilitate a comprehensive comparison of flows and investigate potential changes in particle behavior based on the varying flow conditions.

Single-phase flow with water

The contour plots of the total velocity for Model 1 with an elevated inlet velocity are depicted in Figure 4.8(a). The flow exhibits consistent flow characteristics to the standard flow case, differing by the velocity magnitude. Figure 4.8(a) shows that also, for this case, a significant velocity decrease occurs beneath the ribs.

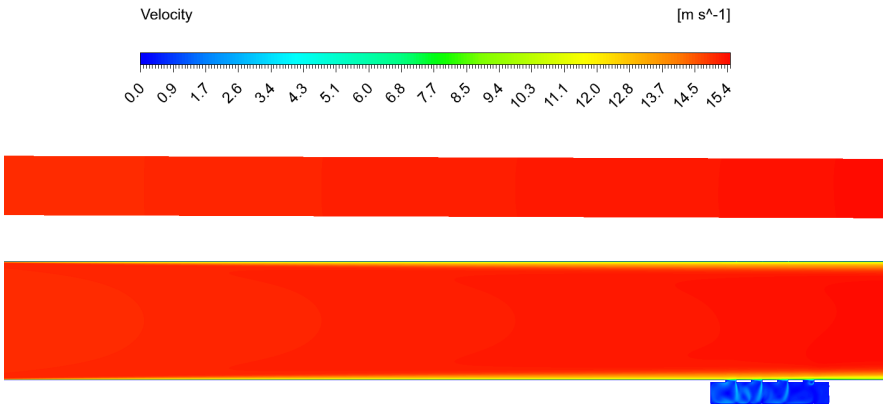

(a) Velocity at the respective planes.

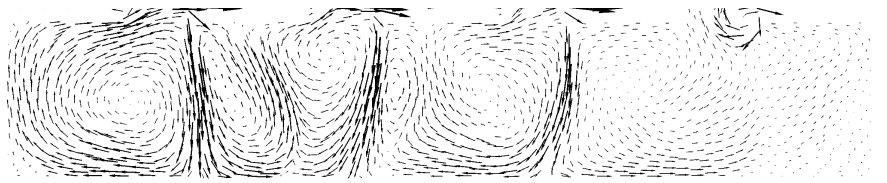

(b) Velocity past the ribs.

Figure 4.8: Velocity contours and trajectories of the elevated flow for Model 1.

In the standard velocity case, the recirculation was stable and exhibited a constant decreasing trend for the ribs further downstream. However, as illustrated in Figure 4.8(b), the recirculation regions for the elevated case appear more irregular. The formation of undefined recirculation patterns is caused by the higher velocity, reducing the residence time within the recirculation region. Additionally, as the flow separates, the flow encounters both a continuation flow in the stream-wise direction and a backflow. With a higher velocity for the passing flow, the continuation-flow regions become more dominating, leading the recirculation zones not to develop completely.

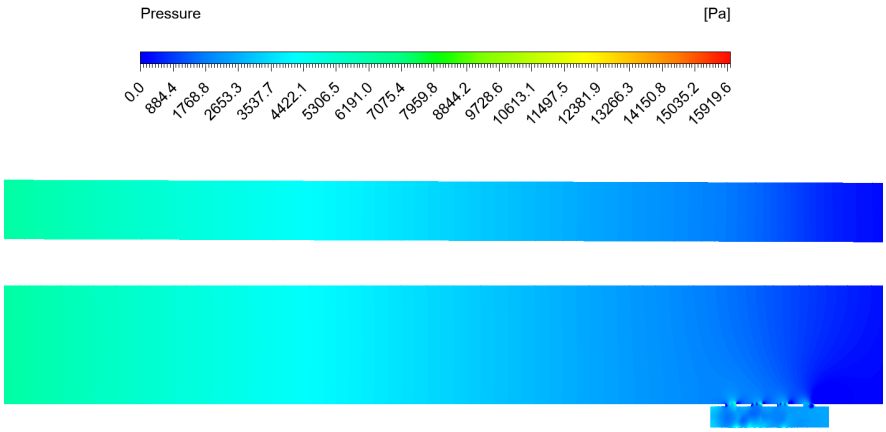

(a) Pressure at the respective planes.

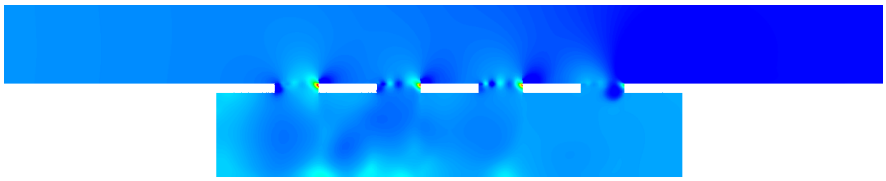

(b) Pressure in the rib section.

Figure 4.9: Pressure contours of the elevated flow for Model 1.

The recirculation region's instability can be attributed to the increased pressure differences over the ribs, as shown in Figure 4.9(b). Unlike the standard velocity case, characterized by a low-pressure zone at the rib opening entrance and a high-pressure zone at the rib opening end, the elevated velocity case exhibits the formation of multiple pressure zones throughout each

rib opening. These pressure fluctuations occur due to heightened shear stress and turbulent energy in the near-wall regions. Immediately downstream of the rib section, the pressure drops further due to the flow separations occurring over the ribs. The flow separations along the tunnel bed result in an acceleration of the flow when reattaching, causing the pressure drop. The accelerated flow negatively affects the particle settlement since particles settle at lower velocities. Figure 4.9(a) shows that the pressure continues to be smooth throughout the tunnel, as it was for the standard flow case.

Multiphase flow with water and particles

The particles are captured at $t = 0.19$ s in Figure 4.10, visually representing the particles' movement and velocity within the flow field. It can be observed that the particles maintain mainly the same features as for the lower inlet velocity, only with a more extensive magnitude. One notable distinction between the flows of different velocities is the amount of particles injected. As the flow velocity increases, the flow requires less time to traverse from the inlet to the outlet. However, the number of particles injected remained the same for both flow cases, resulting in a higher particle flow rate due to the significant reduction in time. The specific details of particle injections are provided in Table 2.2.

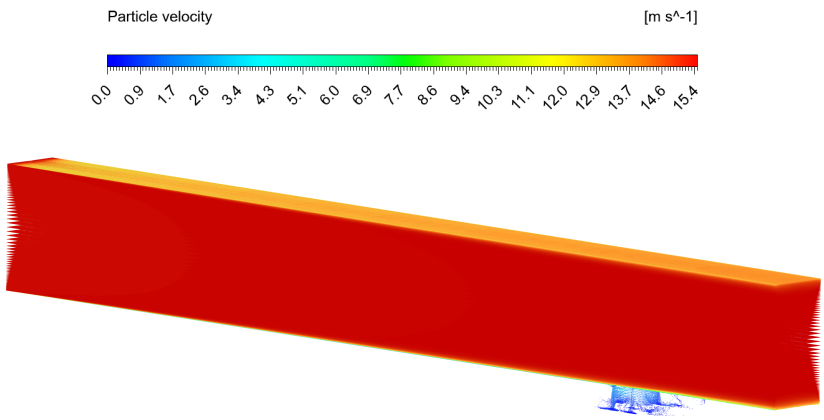

Figure 4.10: Particles and their velocity from the elevated flow for Model 1.

Higher inertial forces push the particles closer to the tunnel surfaces in this elevated flow case. The higher inertial forces are caused by the velocity

increase, leading to higher shear stress and momentum transfer. As shown in Figure 4.11(b), the particles enter through the ribs by the entirety of the rib opening surface. As a result, more suspended particles become trapped beneath the ribs compared to the lower velocity flow. In addition, the varying pressure along the rib opening lead to the trapped particles having a more challenging time escaping, especially for the most upstream rib due to the higher pressure.

A comparison of the particle behavior from the lower velocity flow, depicted in Figure 4.7(a), and in the higher velocity flow, depicted in Figure 4.11(a), shows that due to the higher particle velocity, the particles do not attain a settling velocity, leading them to continue to be transported by suspension and sliding. The only particles obtaining a settling velocity are the particles trapped beneath the ribs.

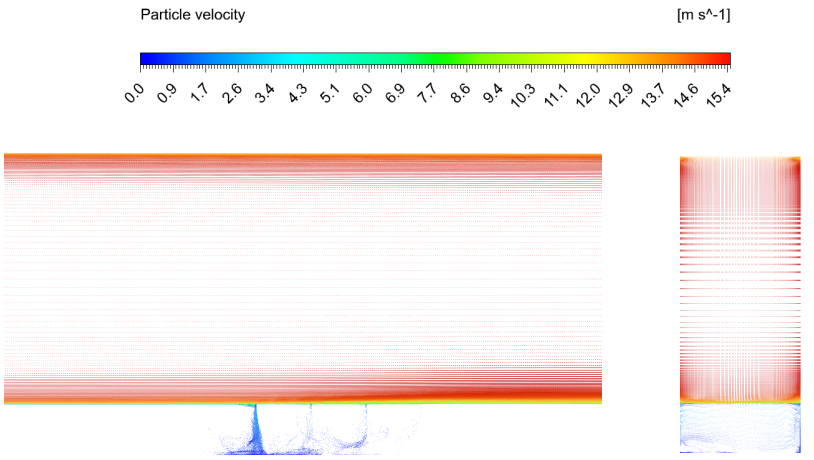

(a) Side view.

(b) Outlet view.

Figure 4.11: Particles and their velocity from a side view and outlet view from the elevated flow for Model 1.

4.3 Model 2

4.3.1 Standard flow case for Model 2

Model 2 introduces a vertical, square cylinder downstream of the inlet. Examining the flow and particle behavior for the current model provides valuable insights into the influence of the cylinder. By studying the flow characteristics, such as velocity, pressure distributions, and vortex formation, it is possible to assess how the presence of the cylinder alters the fluid dynamics and impacts particle trajectories. This understanding enables the opportunity to evaluate the implications for particle settlement, including both favorable and unfavorable aspects.

Single-phase flow with water

A contour of the total velocity of the flow is depicted in Figure 4.12, where the upper plot of Figure 4.12(a) exhibits that the vertical cylinder induces a flow separation, causing vortices to shed downstream of the cylinder. The pressure differences between the front and rear sides of the cylinder generate these vortices, affecting the flow by having regions of varying velocities. An observation is that the vortices exhibit higher velocities in the outer regions and lower velocities in the inner regions. In contrast, the vortices in a laminar or less turbulent flow typically experience higher velocities in the vortex center and lower velocities in the outer regions. However, the interaction between small-scale vortices and large-scale vortices in the flow results in higher velocities in the outer regions of the vortices. The vortices evolve further downstream, leading to fewer velocity fluctuations, giving a reduced flow velocity along the tunnel center. The bottom velocity plot in Figure 4.12(a) shows that the velocity is higher along the centerline than towards the top and bottom of the tunnel. As in Model 1, this occurs due to the no-slip boundaries at the regarding surfaces. From Figure 4.12(b), it becomes evident that the recirculation region is less prominent than for the same velocity in Model 1. This irregular behavior is due to the swirling motion of the vortices across the tunnel centerline, moving the fluid beneath the ribs.

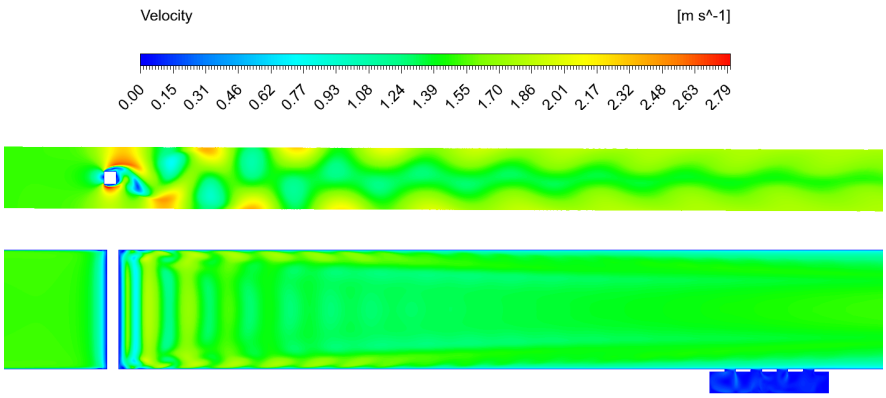

(a) Velocity at the respective planes.

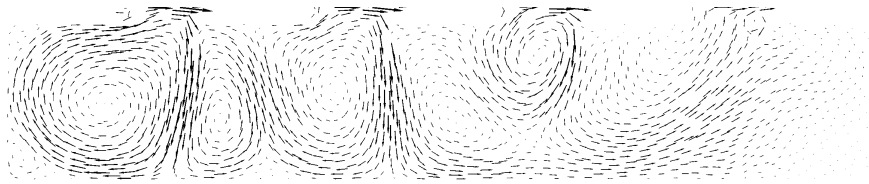

(b) Velocity in the rib section.

Figure 4.12: Velocity contours and trajectories of the standard flow for Model 2.

Figure 4.13(a) depicts that including a cylinder in the tunnel leads to more pressure differences compared to the scenario without the cylinder. Upstream the cylinder, there is a pressure increase in the flow, originating from the placement of the cylinder. The cylinder generates additional resistance in the tunnel when the flow separation occurs due to the pressure zones. To ensure the continuity of the flow in the tunnel, a corresponding increase in pressure occurs upstream of the cylinder to counterbalance the effects of flow separation. Figure 4.13(b) depicts the pressure distribution at the ribs for Model 2, which shares the same pressure characteristics as Model 1. The pressure differentiates with the absence of prominent low-pressure zones beneath the ribs due to the swirling fluid motion.

The turbulent kinetic energy arises from the energy transfer between the mean and turbulent flow, where large-scale vortices interact with small-scale vortices. Also, the interaction between the vortices and the surrounding fluid causes velocity fluctuations and shear stress, enhancing the turbulence

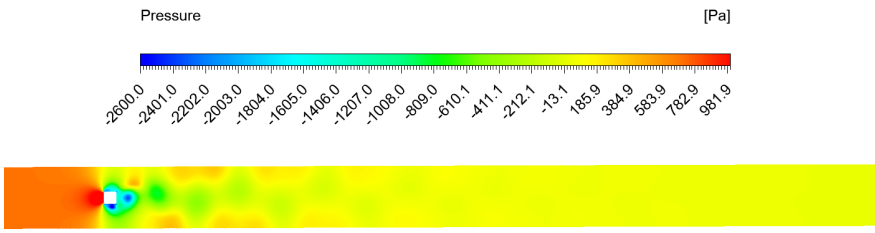

(a) Pressure at the ZX-plane.

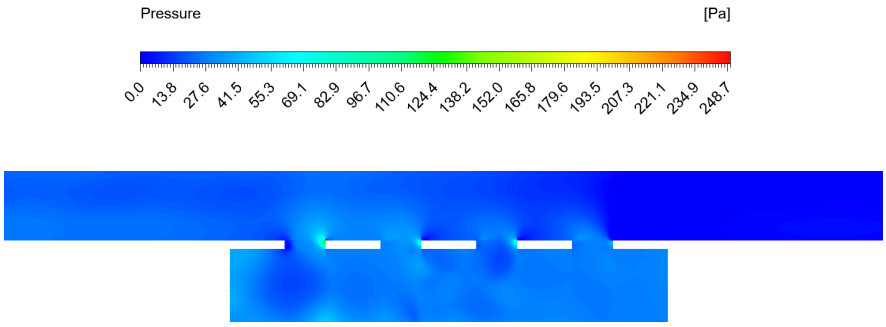

(b) Pressure at the ribs.

Figure 4.13: Standard flow case pressure contour for Model 2.

intensity in the wake region. When observing the generated energy, depicted in Figure 4.14, it becomes visible that the TKE is highly increased in the flow compared to the case with no flow obstruction. Figure 4.14(a) visualize that the TKE is higher in the vortex street than the surrounding fluid due to the energy transport occurring in these regions, leading to lower flow velocity. Figure 4.14(b) shows that the energy through the centerline of the ribs is the same as for Model 1, although the energy towards the tunnel side walls varies slightly from Model 1 due to the flow-swirling motion.

Regarding further downstream development, it is interesting to investigate how the velocity reduces further. By comparing the velocity and TKE, in Figure 4.12(a) and Figure 4.14(a), it is possible to observe that the velocity reduces as the energy dissipates. This creates a flow pattern with a reduced velocity to appear in the tunnel center, whereas the velocity is higher by the tunnel sides.

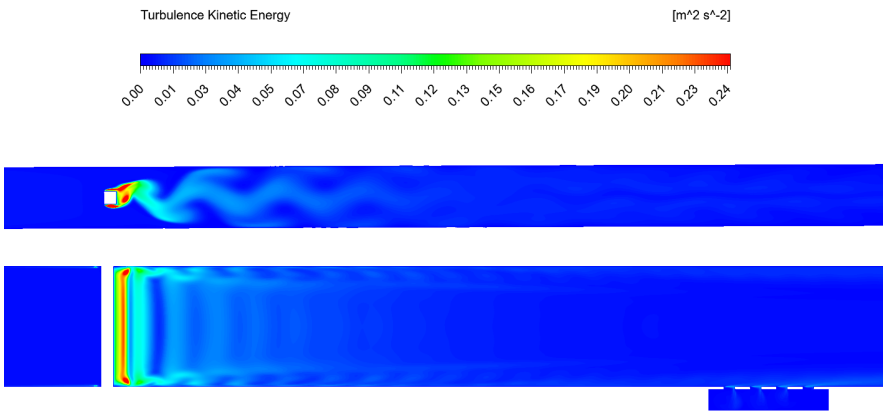

(a) TKE at the respective planes.

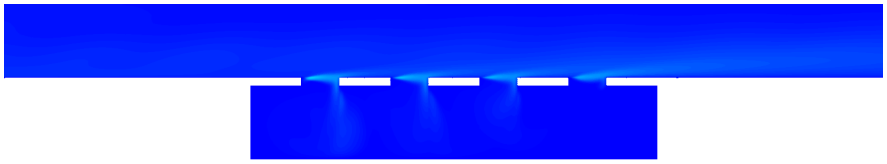

(b) TKE at the ribs.

Figure 4.14: Standard flow case TKE contour for Model 2.

Multiphase flow with water and particles

As for Model 1, it is evident that the particles closely follow the streamlines of the water flow instead of behaving independently. This behavior is observed in Figure 4.15, where the particles are depicted at $t = 1.9$ s after injection start. The particles are suspended in the water, moving with the preferred pathways of the flow. The particles' behavior has changed significantly compared to what was observed in Model 1, shown in Figure 4.6, due to the presence of the cylinder. As the flow progresses downstream, a notable change in behavior can be observed. The flow becomes increasingly influenced by the no-slip conditions at the top and bottom surfaces of the tunnel, leading to enhanced mixing of both the flow and particles towards these surfaces. The mixing can be observed by studying the mass concentration at different locations, presented in Figure 4.17.

In contrast to Model 1 and Model 4, a prominent characteristic of par-

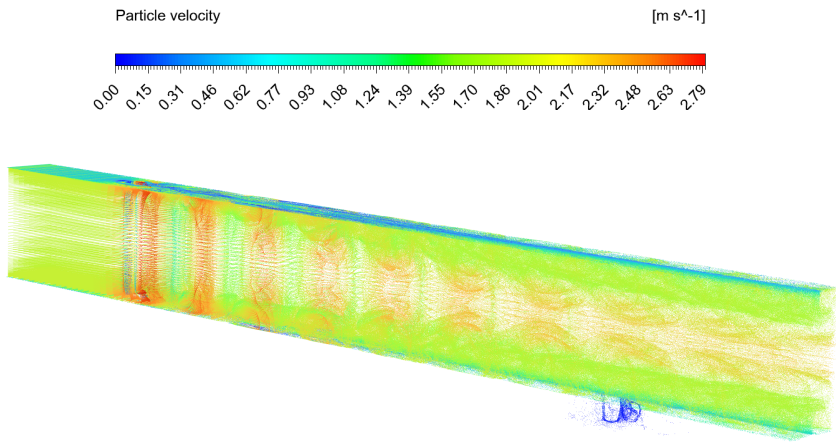

Figure 4.15: Particles and their velocity from the elevated flow for Model 2.

ticles in this model is their symmetrical behavior in both the upper and lower halves of the tunnel, which can be observed from Figure 4.16(a) and Figure 4.16(b). The difference is due to this specific numerical simulation neglecting gravity, causing the particles unaffected by gravitational forces. The particles possess a higher density than the surrounding fluid. Consequently, if gravitational forces were considered, they would surpass the uplifting forces acting on the particles, causing them to settle toward the bottom of the tunnel. This enhances the assumption that gravitation is of importance, even on particles of a smaller size. Although gravity is neglected, more particles enter the ribs for this model than in Model 1. This indicates that having a cylinder may positively affect particle settlement, especially in the case of rib entrance.

Figure 4.17(a) shows the mass concentration through the tunnel's centerline. A distinct feature is particle accumulation in the vortices' outer regions. The swirling motion of the vortices and the heightened velocity in these regions cause the particles to concentrate. Instead of the particles achieving a reduced velocity, they remain entrained in the faster-moving fluid and continue to travel along with the flow. This behavior can be attributed to the inertia of the particles, which makes them less responsive to changes in flow velocity. Such behavior is coherent with the one observed by Nielsen [4] and Burns et. al [13], in which heavy particles concentrate in the vortex edges

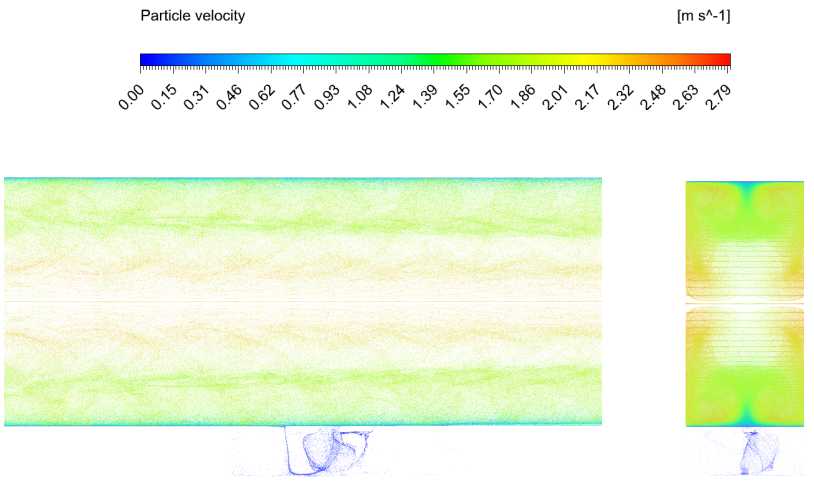

(a) Side view.

(b) Outlet view.

Figure 4.16: Particles and their velocity from a side view and outlet view from the standard flow for Model 2.

and get fast-tracked between the vortices. This phenomenon leads to a less effective settlement of suspended particles, as they will only get reduced velocity once the velocity of the vortex is reduced. Figure 4.17(b) shows the mass concentration of the particles at a location of $y = 0.02$ m over the tunnel bed. It is evident that the no-slip condition at the bottom surface significantly influences the flow and particles. This condition restricts the flow movement, causing the vortices to dissipate earlier than the flow at the tunnel center. Consequently, a mixing process occurs, leading to a more chaotic flow pattern. It can be observed that the mass concentration is also higher at the lower location, suggesting that the dissolving vortices are favorable for particle settlement.

Due to the three-dimensional nature of the turbulent flow in the tunnel, it is essential to analyze the flow characteristics across the entire cross-section. The outlet conditions of the tunnel are visualized in Figure 4.18, providing valuable insights into the flow behavior at the tunnel exit. Specifically, Figure 4.18(a) presents the pressure distribution at the outlet, while Figure 4.18(b) illustrates the streamlines and particle trajectories. By observing the pressure specter of Figure 4.18(a), it is evident that the pressure at the tunnel outlet is significantly lower than the overall tunnel pressure. De-

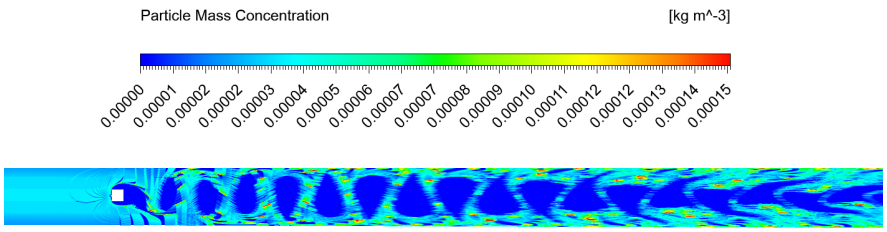

(a) Mass concentration at $ZX = 0.05$ m above the tunnel bed.

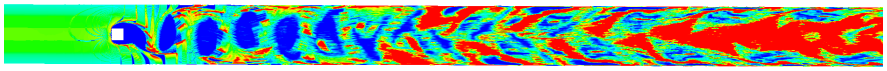

(b) Mass concentration at $ZX = 0.02$ m above the tunnel bed.

Figure 4.17: Mass concentration contours of the standard flow for Model 2.

spite the overall pressure drop through the tunnel, it is essential to note that there are still low-pressure zones at the outlet. Figure 4.18(a) shows that these low-pressure zones are primarily located towards the top and bottom surfaces. The regions of the lowest pressure correspond to the formation of stream-wise vortices, which are generated due to a deceleration of the flow. The deceleration occurs near the surfaces with no-slip conditions and along the tunnel centerline, creating pressure differences that generate vortices. To visualize the flow and particle trajectories, Figure 4.18(b) provides insights into their movement. It can be observed that the flow, and hence the particles, move towards regions of decelerating flow, inducing a swirling motion. This swirling motion is characteristic of vortices in the flow, where the fluid particles rotate around a central axis. These vortices contribute to re-suspending sliding particles at the tunnel bed and introduce them to further particle mixing, which is unfavorable for particle settlement.

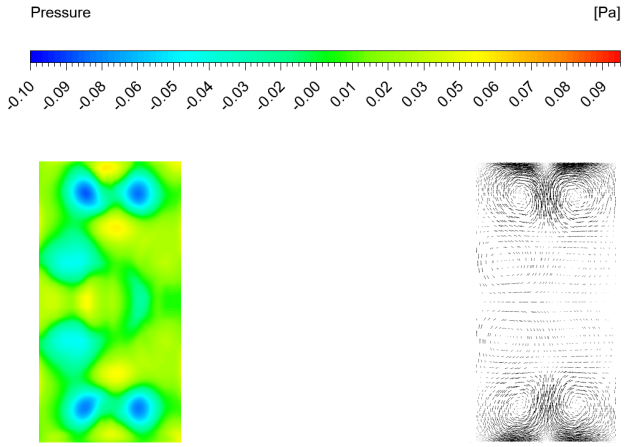

(a) Pressure distribution at the tunnel outlet.

(b) Velocity trajectories at the tunnel outlet.

Figure 4.18: Pressure contour and velocity trajectories at the outlet of the standard flow for Model 2.

4.3.2 Elevated flow case for Model 2

Model 2 was simulated with an increased inlet velocity to explore the influence of altered flow conditions on the behavior and distribution of the particles.

Single-phase flow with water

Figure 4.19 displays the contour plot of the total velocity for Model 2 with an elevated inlet velocity. The upper plot of Figure 4.19(a) demonstrates that the flow exhibits vortex shedding, similar to the case with a lower velocity. However, the shedding pattern appears more irregular and chaotic. Unlike the smooth and diminishing pattern observed in the lower velocity case, the vortex shedding here shows greater velocity fluctuations and a less predictable and decaying pattern.

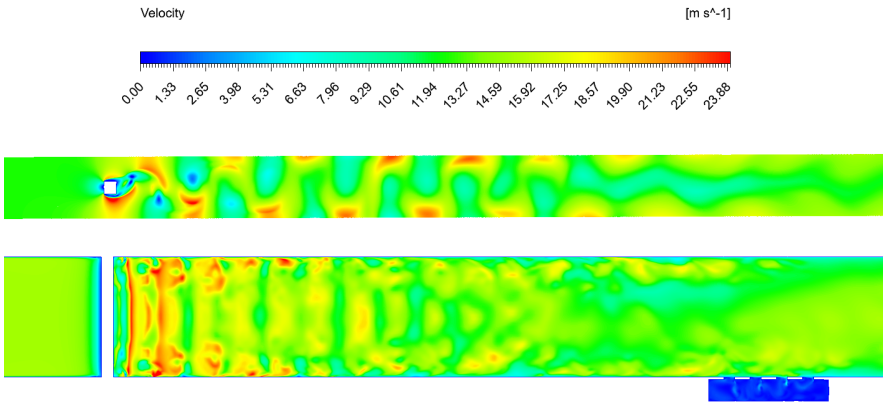

(a) Velocity at the respective planes.

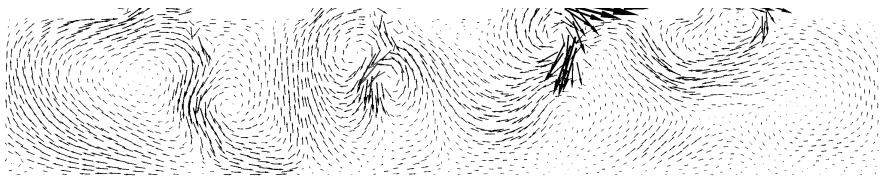

(b) Velocity in the rib section.

Figure 4.19: Velocity contours and trajectories of the elevated flow for Model 2.

The lower plot of Figure 4.19(a) shows that the flow experiences mixing through the channel, which decays further downstream. The enhanced velocity fluctuations lead to particle mixing, preventing particle clustering. The absence of particle clustering in a sand trap is beneficial as it allows smaller particles to enter the turbines, resulting in less damage. However, the elevated particle mixing is also unbeneficial, as it re-suspends and hinders the particles from reaching their settling velocity.

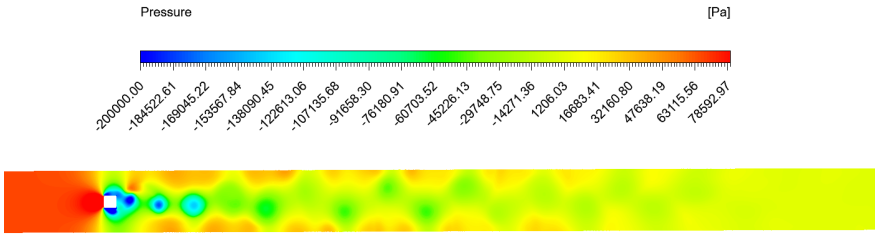

(a) Pressure at the ZX-plane.

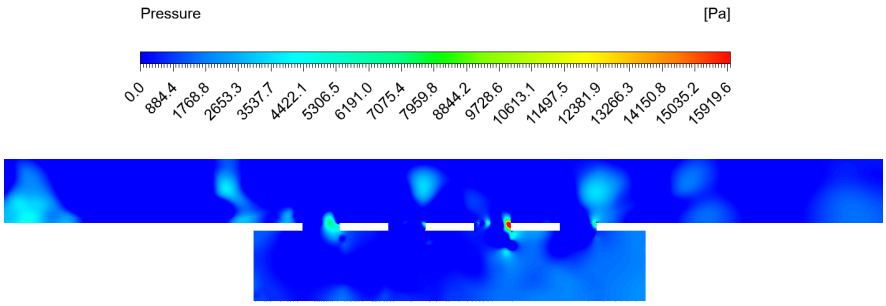

(b) Pressure in the rib section.

Figure 4.20: Pressure contours of the elevated flow for Model 2.

The flow velocity and trajectories over the ribs, as depicted in Figure 4.19(b), shows that the shedding frequency is sufficiently high to cause irregular flow beneath the ribs. This is seen by the velocity trajectories not developing any distinct recirculation zones, as in the lower-velocity flows. The irregular flow behavior results in mixing of settled particles, potentially causing settled particles to be entrained back into the tunnel flow. By examining Figure 4.20(b), it becomes evident that the pressure distribution varies compared to the elevated flow case for Model 1, despite having the same pressure spectrum. The current case has a lower pressure, and the pressure

does not have any distinct patterns. Figure 4.20(a) shows that the vortices do not dissolve as rapidly as for the standard flow of Model 2, which will cause particles to be transported in the outer regions of the vortices further downstream.

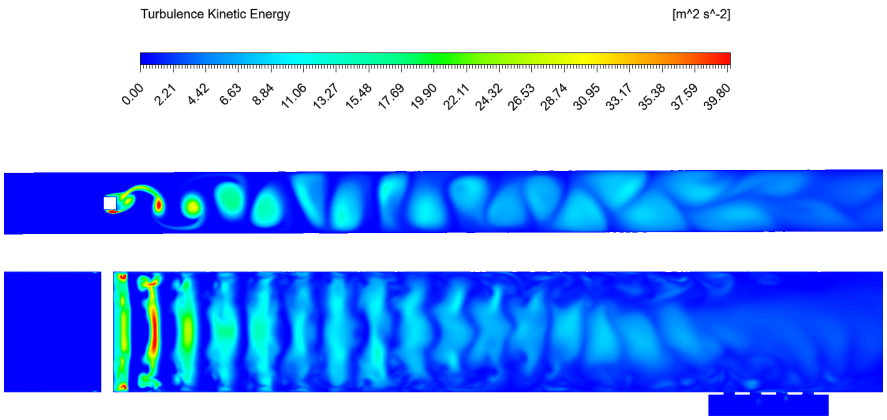

(a) TKE at the respective planes.

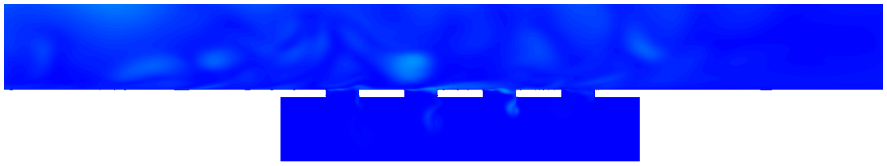

(b) TKE in the rib section.

Figure 4.21: TKE contours of the elevated flow for Model 2.

In Figure 4.21(a), it is evident that a higher velocity generates more TKE. The elevated levels of TKE are attributed to the increased turbulence intensity and higher levels of shear and momentum in the fluid. Additionally, the increased TKE is due to a higher flow velocity imparting more energy to the fluid, generating more vigorous vortices. However, as the vortices in the flow enlarge, the TKE decreases due to energy dissipation, where the energy from strong vortices is dissipated to smaller surrounding vortices in the fluid. This dissipation mechanism causes energy redistribution within the flow, decreasing TKE as the vortices evolve, as is observed from both the upper and lower plot of Figure 4.19(a). Reduced levels of TKE further

downstream are beneficial for particle settlement, as it is coherent with a reduced flow velocity.

When comparing the standard and elevated cases of Model 2, the results indicate that the standard case is more beneficial for optimal particle settlement. The reduced particle settlement in the elevated flow is due to greater mixing, high inertial forces, and more energy, preventing the particles from reaching a settling velocity as they traverse through the tunnel.

4.4 Model 3

4.4.1 Standard flow case for Model 3

To further understand the flow dynamics, Model 3 was introduced, which incorporates three vertical square cylinders within the tunnel flow. The decision to investigate this model was motivated by the desire to explore the interaction between the growing vortices generated by multiple cylinders and how it impacts the behavior of suspended particles. Model 3 is highly relevant concerning installations in a sand trap, primarily due to its size, making it more realistic to have multiple FCS.

Single-phase flow with water

Figure 4.22 depics the contours of total velocity for Model 3. By observing the velocity in the top plot of Figure 4.22(a), it is noticeable that the wake downstream of the cylinder has increased compared to that of Model 2. The wake prolongation for the center wake occurs as vortices from the outer cylinders merge with the vortices of the center cylinder. In contrast, the vortices for the outer cylinders are only influenced by the center cylinder vortices. It can also be observed that the flow is symmetric along the tunnel centerline due to the current model having an odd number of cylinders. As the flow progresses downstream of the wake regions, vortices begin shedding.

By comparing the outlet conditions of Model 2, shown in Figure 4.12(a), and Model 3, shown in Figure 4.22(a), it is evident that they differ. In Model 2, there is a small area along the centerline where the flow velocity is reduced, leaving a gradual velocity decrease towards the tunnel side walls. In contrast, for Model 3, it can be observed that the reduced velocity along the tunnel centerline has a broader area, having a more sudden decrease in velocity closer to the tunnel side walls. This results in the flow, and hence the particles, having a larger area of reduced velocity upon entering the rib openings. Such a velocity reduction is beneficial, as it increases the possibility for particles to enter the rib openings over the entirety of the opening surface.

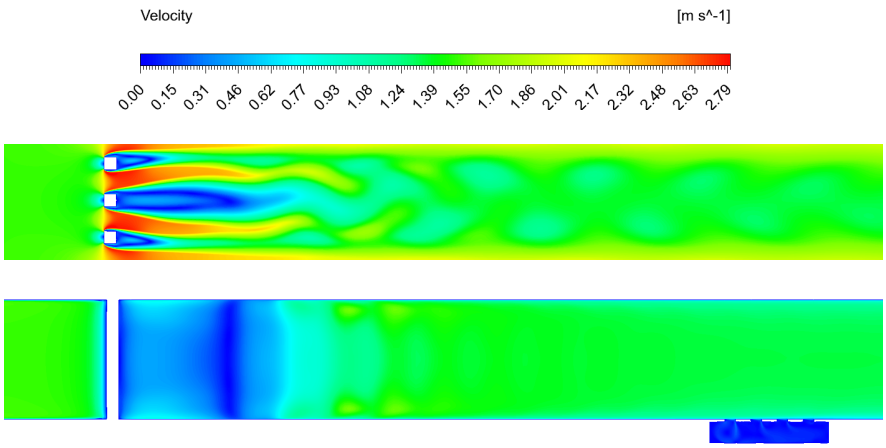

(a) Velocity at the respective planes.

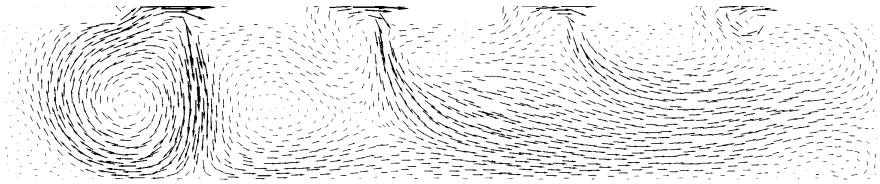

(b) Velocity in the rib section.

Figure 4.22: Velocity contours and trajectories of the standrad flow for Model 3.

From Figure 4.22(b), it is evident that there is only a clear recirculation zone beneath the first rib. The flow over the rib openings further downstream encounters a separation, where most flow continues in the streamwise direction beneath the ribs. The flow experiences this motion due to a weak swirl over the centreline, in which the trajectories are depicted. The movement slightly overpowers the pressure zones compared to Model 1, but not as much as the swirling motion for the standard case in Model 2. This is favorable for particle settlement as it decreases the probability for particles to escape after completing a recirculation.

It is also of interest to examine the vortex development further downstream. The TKE distribution, as depicted in Figure 4.23, reveals several distinct characteristics that differentiate it from the flow pattern observed for Model 2. As previously mentioned, the presence of multiple cylinders in

the flow leads to an interesting phenomenon where the wake is prolonged due to the interaction of vortices. However, unlike the case of a single cylinder where the flow reattaches in the cylinder wake, the flow does not reattach as effectively when multiple cylinders are present. From the upper plot of Figure 4.23(a), it becomes evident that the lack of reattachment leads the flow to have six separate regions with heightened TKE. The vortices downstream of the two outermost wakes remain nearly unaffected by the innermost vortices, creating a constant energy level towards the side walls. The vortices shed from the four inner wakes interact immediately, creating one vortex street down the tunnel center with increased TKE. The increased TKE is unbeneficial regarding particle settlement, as the particles will remain suspended longer in higher energy flows.

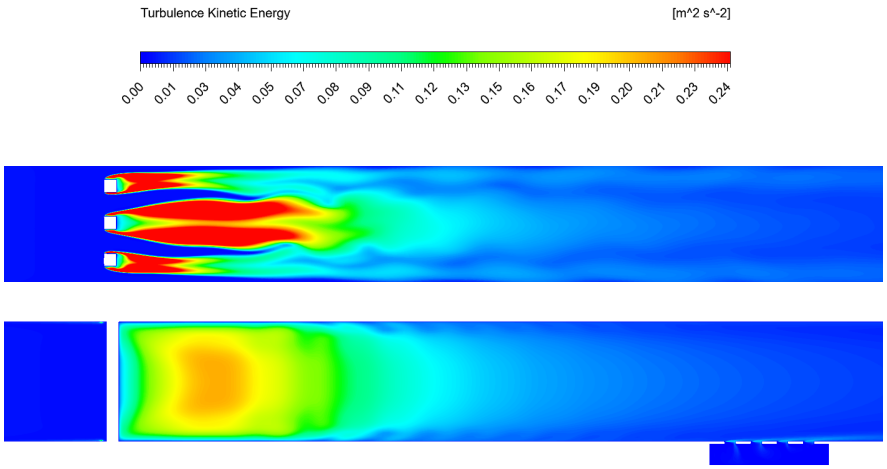

(a) TKE at the respective planes.

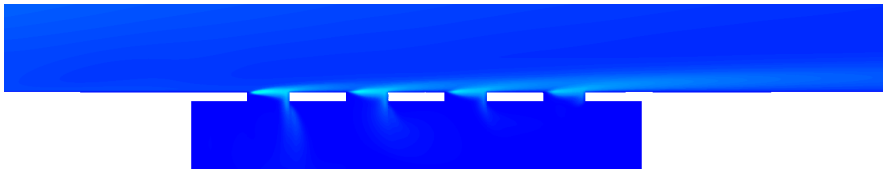

(b) TKE at the rib-section.

Figure 4.23: TKE contours of the standard flow for Model 3.

When assessing the mass concentration for Model 2, depicted in Figure 4.17, it was shown that the particles gather in the outer regions of the vortices. Concerning particle gathering in the tunnel flow with three cylinders, they will therefore gather similarly due to the same conditions. If the flow and particle characteristics resemble that of Model 2 and Model 3, the particles will closely follow the flow pattern.

4.5 Model 4

4.5.1 Standard flow case for Model 4

Numerical simulations were conducted with Model 4, incorporating a vertical circular cylinder downstream of the inlet. The objective was to examine the impact of different cylinder geometries on flow and particle behavior, aiming to optimize and identify the most favorable geometry for particle settlement in a sand trap.

Single-phase flow with water

Figure 4.24 shows the contour plots of the total velocity for flow past a circular cylinder. The velocity specter is similar to Model 2, involving flow past a square cylinder.

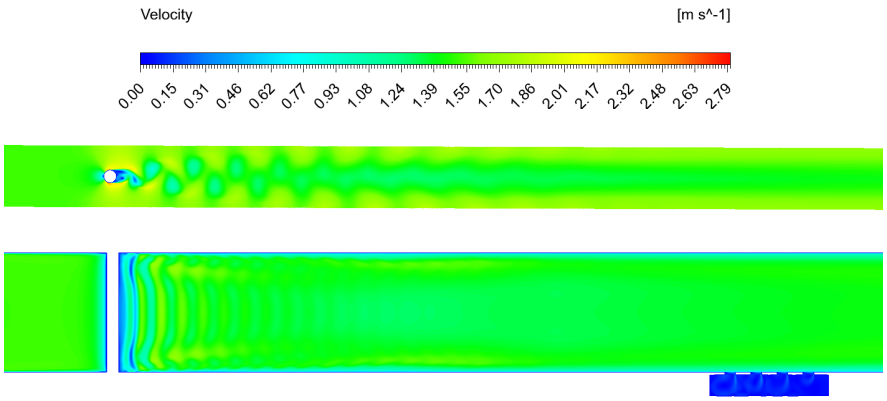

(a) Velocity at the respective planes.

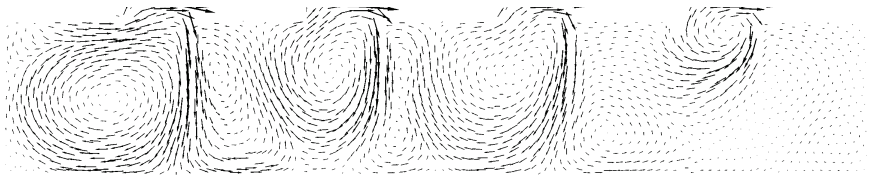

(b) Velocity in the rib section.

Figure 4.24: Velocity contours and trajectories of the standard flow for Model 4.

Figure 4.24(a) shows that compared to Model 2, Model 4 has less amplified velocity differences, resulting in the downstream vortices dissolving earlier. Consequently, a more significant portion along the tunnel center has a reduced velocity for this model. The vortices dissolving earlier originates from the flow separation at the cylinder walls. For the square cylinder, the flow exhibits a more rapid stagnation at the front side of the cylinder, separating the fluid instantly. The circular cylinder's flow separation occurs more smoothly as the pressure gradients along the cylinder side walls change gradually. As the flow decelerates near the circular cylinder surface and accelerates further out, the APG reaches a point at the cylinder where the pressure forces dominate the inertial forces, leading to a smooth separation. This results in smaller vortices being shed at a higher frequency downstream of the circular cylinder than the square cylinder, which exhibits larger vortices at a lower shedding frequency.

Figure 4.24(b) depicts the flow trajectories over the ribs. It is evident that as the flow progresses downstream, the prominence of vortex shedding diminishes, resulting in a reduction of swirling motion across the tunnel centerline. This, in turn, leads to the formation of stable recirculation regions beneath the ribs, similar to what was observed for the standard flow case of Model 1. The velocity plot for the standard case of Model 1, shown in Figure 4.3 demonstrated that the velocity decreased towards the side walls and increased along the tunnel center. In the current model, shown in the upper plot of Figure 4.24(a), it is observed that the velocity toward the tunnel side walls is slightly higher than for Model 1. The center section has a slightly lower flow velocity, making Model 4 beneficial for the particles reaching their settling velocity. A further velocity reduction is favorable for the particles to enter through the entirety of the surface opening of the ribs.

The pressure variances through the tunnel are shown in Figure 4.25(a), with the same scale as for Model 2, shown in Figure 4.13(a). For Model 4, the regions containing pressure differences are smaller than for Model 2. This amplifies the notation that the vortices being shed are smaller and shed at a higher frequency. In contrast, the pressure of the flow past the ribs behaves differently than for Model 2. The pressure contour for the flow over the ribs, with the same scale as for the standard flow cases of Model 1 and Model 2, is depicted in Figure 4.25(b). The region beneath the ribs has the same behavior as the pressure in Model 1, only that the low-pressure zones are further amplified for Model 4. The even lower pressure generates a stronger suction of particles beneath the ribs, potentially leading more particles to enter and settle.

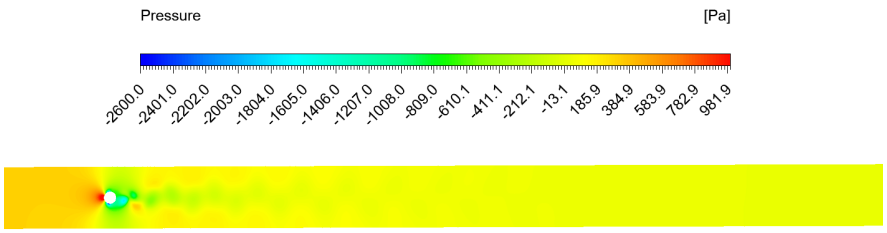

(a) Pressure at the ZX-plane.

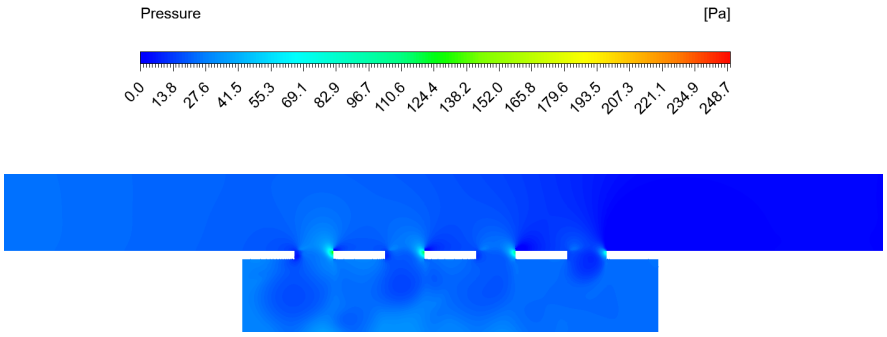

(b) Pressure in the rib section.

Figure 4.25: Pressure contours of the standard flow for Model 4.

The turbulent kinetic energy of the flow is depicted in Figure 4.26. The top plot of Figure 4.26(a) shows that energy dissipation mainly occurs within the vortices, while the regions between the vortices exhibit minimal energy dissipation. This distribution differs from the observations of Model 2, shown in Figure 4.14, where the TKE distribution is more coherent. The abruptions in TKE affect suspended particles transported in the outer regions of the vortices by causing them to be released from the flow pattern. As a result, the released particles have a higher probability of settling earlier, as they are no longer subjected to the continuous swirling motion and energy dissipation within the vortices.

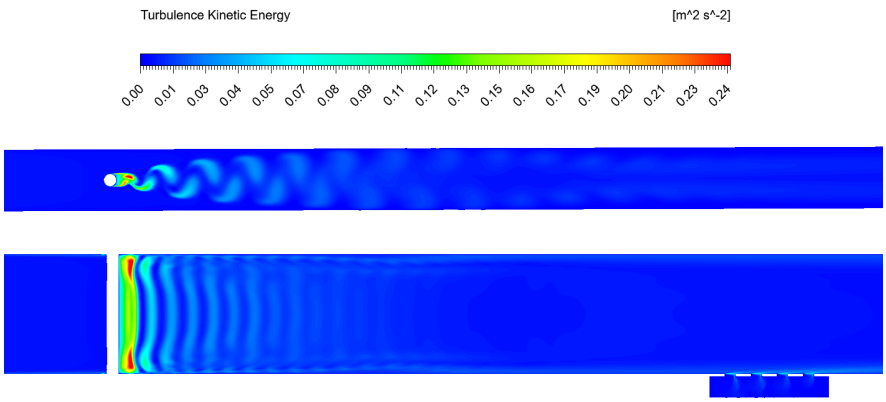

(a) TKE at the respective planes.

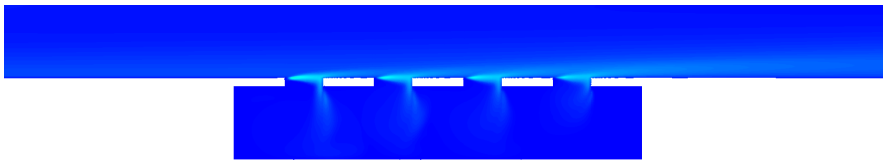

(b) TKE in the rib section.

Figure 4.26: TKE contours of the standard flow of Model 4.

Multiphase flow with water and particles

Figure 4.27 shows the particles and their velocity at $t = 1.9$ s after injection start for Model 4. From Figure 4.27, it becomes evident that the particles still follow the flow pattern closely, indicating that the hypothesis that the particles' behavior is closely related to the flow behavior, based on a low Stokes number, is correct. A noticeable difference from Model 4, in which the gravity was neglected, is that the particles do not behave symmetrically in the upper and lower half of the tunnel for the current model. Additionally, more particles are trapped beneath the ribs. Both these findings are attributed to the importance of gravity in particle settlement.

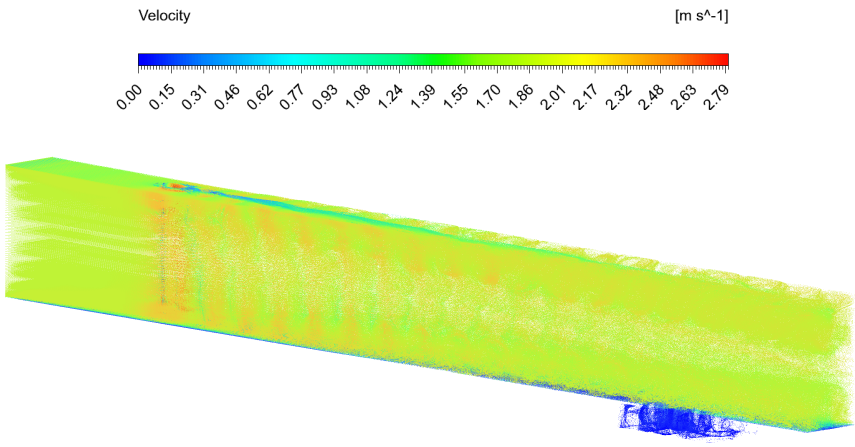

Figure 4.27: Particles and their velocity from the standard flow for Model 4.

For Model 4, there is a considerably higher amount of particles trapped beneath the ribs compared to both Model 1 and Model 2. This occurrence is due to multiple factors. Firstly, from Figure 4.28(a) and Figure 4.28(b), it is evident that the particles in Model 4 are entering the ribs mainly from the tunnel center. In contrast, the particles mainly entered the ribs by the side walls in Model 1. This difference originates from the flow, and hence the particles, being more affected by the flow pattern in Model 4, while they are only affected by the inertial forces in Model 1. Secondly, the gravity was neglected for Model 2, resulting in the particles not overcoming the exerted lift forces. If gravity were included, the particles would behave more likely

as they do for Model 4. However, the velocity is further reduced in Model 4, resulting in more particles entering the ribs. The developing stream-wise vortices also lead the particles to settle along the tunnel center. This, in combination with the increased pressure drop beneath the ribs, leads more particles to enter through the ribs by the suction effect.

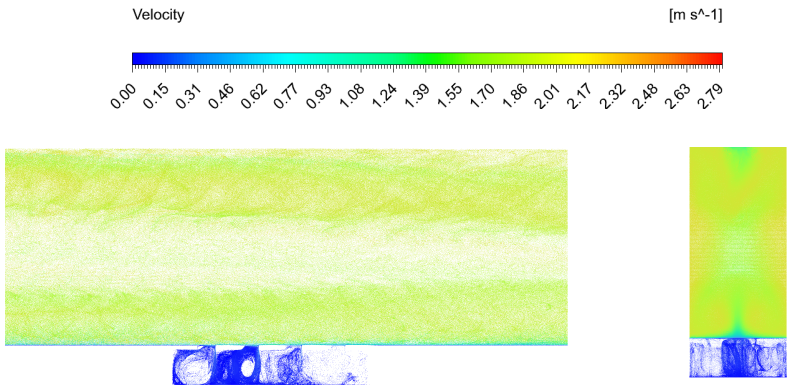

(a) Side view.

(b) Outlet view.

Figure 4.28: Particles and their velocity from a side view and outlet view from the standard flow for Model 4.

From Figure 4.28(b), it is evident that the stream-wise vortices in Model 4 are more developed than in the case of Model 2. The further development is due to the cylinder-induced vortices dissolving earlier, leading the no-slip condition to have a more considerable effect. Further investigation is obtained by comparing this particle behavior with the pressure and particle trajectories, shown in Figure 4.29(a) and Figure 4.29(b), respectively. It can be observed that the vortices generated by the cylinder are nearly entirely dissolved at the outlet, meaning only the stream-wise vortices contribute. This alteration in the flow pattern leads to reduced complexity and mixing of the turbulent flow, which can be seen from Figure 4.29(b). The particle trajectories in Model 2, shown in Figure 4.18(b), showed that the particles followed both stream-wise vortices and cylinder-induced vortices. In contrast, the particle trajectories for Model 4 show that only the stream-wise vortices remain. These vortices are anticipated to converge and dissipate as they progress further downstream, resulting in the particles being released and able to settle.

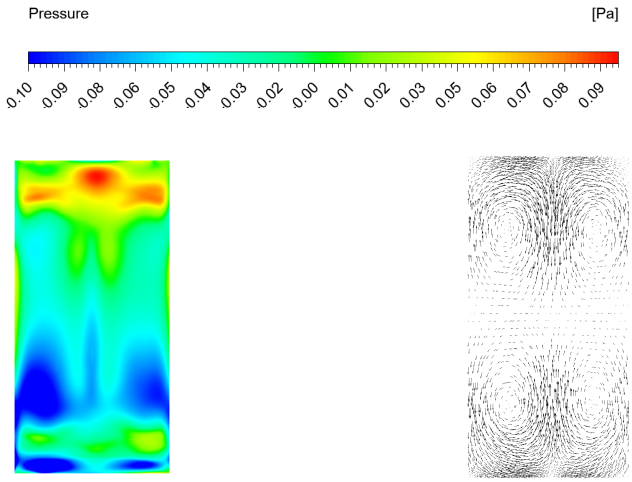

(a) Pressure distribution at the tunnel outlet.

(b) Velocity trajectories at the tunnel outlet.

Figure 4.29: Pressure contour and velocity trajectories at the outlet of the standard flow for Model 4.

For Model 4, Figure 4.30(a) shows the mass concentration trough the tunnel centerline, and Figure 4.30(b) shows the mass concentration at $y = 0.02$ m above the tunnel bed. The particles suspended in the tunnel center are transported in the outermost regions of the vortices, as well as outside the vortex street. The vortices dissipate as the flow progresses downstream, and the particles are subjected to the no-slip conditions of the top and bottom surfaces. It becomes evident that the particles at $y = 0.02$ m are affected by the no-slip condition at an earlier stage than the particles through the tunnel center. The earlier influence results in the earlier mixing of the flow and the particles. This mixing can be further validated when investigating the pressure in Figure 4.29(a). It can be seen that pressure zones of a low magnitude are forming, indicating that the pressure differences are decaying.

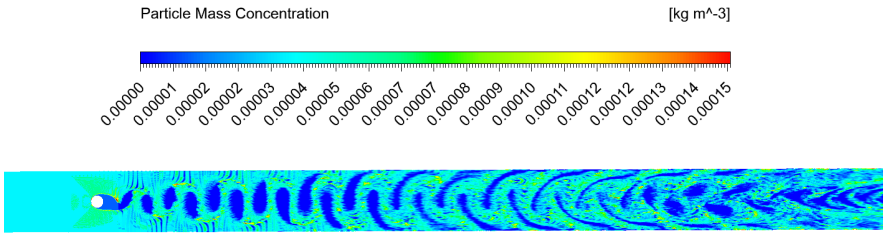

(a) Mass concentration at $ZX = 0.05$ m above the tunnel bed.

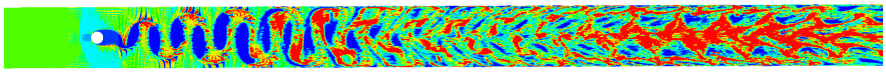

(b) Mass concentration at $ZX = 0.02$ m above the tunnel bed.

Figure 4.30: Mass concentration contours of the standard flow for Model 4.

4.6 Model 5

4.6.1 Standard flow case for Model 5

The smaller vortices shedding at a higher frequency for the circular cylinder than the square cylinder made it interesting to investigate how the vortices from multiple circular cylinders interact. The following section focus on a comparison between Model 3, having three square cylinders, and Model 5, having three circular cylinders.

Single-phase flow with water

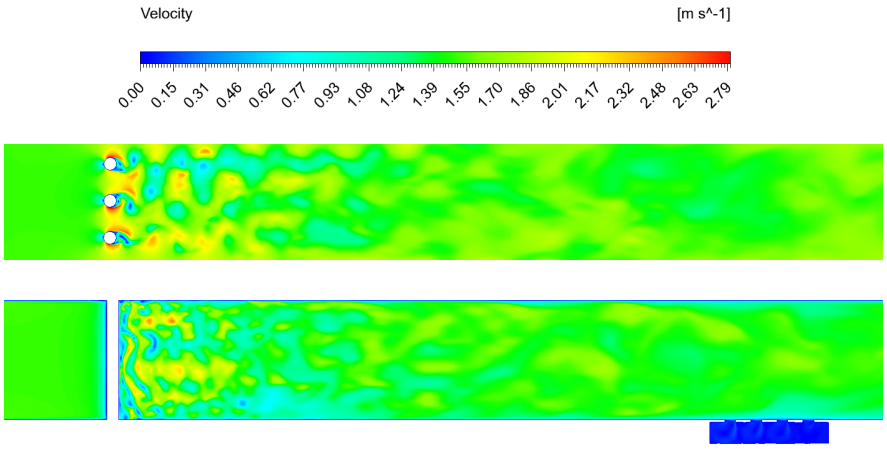

(a) Velocity at the respective planes.

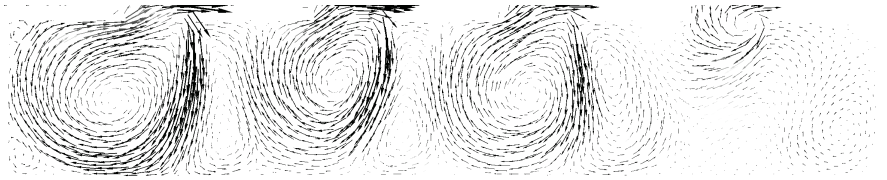

(b) Velocity in the rib section.

Figure 4.31: Velocity contours and trajectories of the standard flow for Model 5.

Figure 4.31(a) depicts the contour of the total velocity for the flow past three circular cylinders. The upper plot shows that vortices' smaller extent

prevents them from early interactions and from prolonging the wake region, as was seen for Model 3. Consequently, the vortices immediately downstream of the cylinder exhibit greater velocity fluctuations, as evidenced by the lower plot in Figure 4.31(a). As the flow progress downstream, the vortices gradually enlarge and dissipate, eventually merging and giving rise to an irregular flow pattern. The intensified velocity fluctuations and irregular flow pattern result in earlier mixing of particles. However, this mixing proves unfavorable since it leads to prolonged particle suspension.

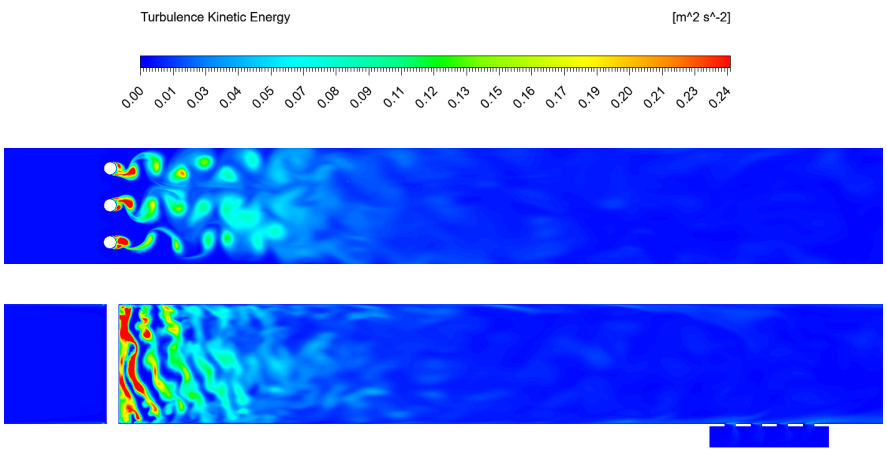

(a) TKE at the respective planes.

(b) TKE in the rib section.

Figure 4.32: TKE contours for the standard flow of Model 5.

Further comparison between the different models is investigated by observing the turbulent kinetic energy, depicted in Figure 4.32. The upper energy plot in Figure 4.32(a) demonstrates that TKE obtained by the vortices is initially high immediately downstream of the cylinders. However, as the vortices grow and mix, the energy diminishes rapidly, reducing the velocity, as seen in Figure 4.31. Compared to Model 3, the reduction in TKE

at the rib section, as observed in Figure 4.31(b), validates the decrease in velocity observed in Figure 4.32(b). The coherence between the reduction in TKE and the decrease in velocity further supports this validation.

4.7 Particle attributes in a sand trap

This section will discuss the results regarding particle settlement in a hydropower sand trap. It will include a closer comparison of the most relevant features discovered to discuss which design is optimal for the settlement.

The cases investigated with a single-phase flow, followed by a multiphase flow, showed that the particles do not influence the water to a significant degree. The Stokes numbers, as provided in Table 3.1, suggested that the particles would have minimal or negligible impact on the flow, which was confirmed. The flow through a sand trap will consist of sediments of various sizes, while this experiment has only examined the smallest sand particles. While the particles in this study do not exhibit clustering or influence each other, it should be noted that larger sediments and particles could affect them in a sand trap. These attributions vary with the sediments' size and density, sediment volume, and flow characteristics.

The different flow cases in Model 2 and Model 4 showed variations in shedding frequency. In Model 2, the standard flow case had a shedding frequency of 39.8 Hz, while the elevated flow case had a shedding frequency of 481.9 Hz. Model 4 exhibited a shedding frequency of 57.9 Hz for the standard flow. Model 3 exhibits the same shedding frequency as Model 2, and Model 5 exhibits the shedding frequency as Model 4. Although the shedding frequency does not affect the particle settlement, it describes the flow characteristics that have an effect. A higher shedding frequency indicates a more turbulent flow, resulting in prolonged particle suspension. Conversely, a lower shedding frequency suggests a lower level of turbulence, enabling particles to reach their settling velocity quicker. Regarding this study, it is desired to evaluate the optimal cylinder geometry for an FCS in a sand trap. Model 4 favors single-cylinder cases due to the faster-decaying vortices and reduced outlet velocity. In contrast, Model 3 is preferred for multiple-cylinder cases because the merging vortices form a stable and repeating pattern. This results in particles following the flow pattern and reducing their velocity in Model 3, while in Model 5, the irregular pattern leads to further particle mixing.

Due to several contributing factors, the particles investigated in the current study did not exhibit a settling velocity. A crucial factor is the design of the simplified model, lacking the essential features of a sand trap. A pressurized sand trap would have a larger cross-sectional area than the headrace tunnel and the penstock, reducing flow velocity upon entrance. The models studied have a constant cross-section, hence neglecting this feature. Fur-

thermore, a sand trap has no-slip boundaries and roughness for all surfaces, creating shear and friction forces, which are not incorporated into the simplified models. Lastly, the tunnel length is reduced compared to a sand trap due to the investigation primarily focusing on flow and particle interactions and minimizing computational requirements.

This study applied two relatively high inlet velocities to the models, focusing on comparison and flow characteristics. It extends previous research by selecting inlet velocities based on relevant parameters and information from existing literature. The standard flow case offers a more accurate depiction of a sand trap's inlet velocity than the elevated case, specifically for the hydropower plant in previous research. Regardless, the elevated flow case remains valuable as it offers important insights and information for the flow characteristics.

Chapter 5

Conclusions

To minimize erosion and extend the hydroturbine lifespan, it is vital to properly remove sediments incoming with water flow. A sand trap is designed to facilitate the particles to achieve their settling velocity, reducing the deposits to the turbines. A numerical study investigating flow past flow calming structures has been conducted to optimize the sand trap designs, primarily focusing on flow and particle interactions. Five models, each representing a simplified version of a sand trap with an upgraded design, were created to facilitate the research. The models include zero, one, and three structures having a square and circular geometry. A grid convergency index study was carried out for Model 2 to reduce the discretization error, and the same discretization approach was applied to the remaining models. Both single-phase and multiphase simulations were conducted on these models, utilizing water and particles of a uniform size. The simulations were transient, allowing the time-dependent flow features to be generated.

The results obtained for the base model cases show that particles closely follow the streamlines of the flow. The particles exhibit consistent behavior with the flow, confirming the validity of the Stokes number assumption regarding the coupling between the flow and particles. The velocity is sufficiently high for both the standard and elevated case to transport particles by suspension and sliding, impeding settlement at the tunnel bed. Therefore, obtaining a similar flow velocity and tunnel length is essential to estimate the specific trap efficiency for the upgraded designs. The inertial forces affect the particles to have equal trajectories in the same directions, inhibiting clustering. Models with a single cylinder further confirm the highly coupled multiphase flow. The cylinder, representing a flow calming structure, induces flow separation, generating a vortex street for all models. Particles follow the outer regions of vortices, mixing as they dissolve. Gravity is essential to

uphold the correct separation of particles, allowing the particles to approach the tunnel bed.

To conclude, the behavior of sand particles of the considered size and density relies heavily on the flow pattern. Achieving optimal sedimentation requires reducing the flow velocity to a point where the gravitational forces acting on the particles outweigh the inertial forces of the flow. Introducing vortices to the flow generates particle mixing, particularly benefiting particles suspended near the upper surface of the tunnel. The enhanced mixing redirects particles away from the walls, thereby increasing their probability of reaching the free stream in the tunnel center. The results from Model 4 show that there is a reduced flow velocity in the tunnel center, making it beneficial for particles to be led there. The particle results obtained from the standard case of Model 1 and Model 4 demonstrate this mixing and the difference in particle distribution towards the upper surface. A circular flow calming structure alone optimizes the sand trap design, while square ones are advantageous in parallel. Higher levels of flow turbulence in the context of flows past flow calming structures correspond to heightened turbulence intensity and increased velocity fluctuations, leading to increased mixing within the flow. However, a lower turbulence flow is more favorable for optimal particle settlement as it increases the likelihood of a smoother and decaying vortex street. The ribs beneath the tunnel bed proves beneficial for sand particle capturing, and adjusting the openings after the specific flow velocity would increase its efficiency.

The settling velocity of the examined particles is determined to be $\omega_0 = 0.095$ m s^{-1}, and the particles must encounter this velocity to settle fully. The flow beneath the ribs is the only region where this requirement is consistently met. In a final conclusion, smooth vortices contribute beneficially to moving higher-located suspended particles downward, consequently relocating lower particles further above the tunnel bed. Adjustments to the tunnel bed and the development of the ribs would be necessary to increase particle settlement further.

Chapter 6

Future work

For future studies, exploring multiple scenarios more in-depth would be beneficial. Acquiring and incorporating realistic measures of flow and particle velocities would be advantageous, as well as revisiting the design of the sand trap to ensure realism. Continuing the turbulent flow investigations at lower velocities could also be possible, examining whether the flow velocity promotes increased particle settling or if the settlement remains consistent compared to higher-velocity flows. Additionally, applying no-slip boundaries and surface roughness would be valuable. Conducting these numerical studies with a realistic sand trap design would help assess the impact and cooperation of these conditions.

Exploring alternative designs for the ribs is also of interest. The current study revealed particles entering the ribs primarily through the first three rib openings due to the higher pressure drop beneath the opening, suggesting that increasing the number of ribs may not be necessary. Instead, optimizing the design could involve introducing sections of tree rib openings at different locations in the tunnel and maintaining adequate spacing between them. Such a design allows suspended and saltating particles immediately downstream the ribs to move downwards to the tunnel bed and start sliding before entering a new rib section. Additionally, incorporating a second layer of ribs could enable more particles to settle beneath the ribs by reducing the likelihood of reintroducing the particles to the tunnel flow by the recirculation. The second rib layer could be staggered, further trapping the sediments.

References

[1] Wolfgang, R., Vereide, K., Mauko, G., Havrevoll, O. H., Schneider, J., and Zenz, G., 2021, "Retrofitting of pressurized sand traps in hydropower plants," Water, **13**(18), pp. 13,2515.

[2] Stjern, R. J., 2022, "Study of sand trap mechanism in a hydropower plant," Project work, NTNU.

[3] Maxey, M. t. and Corrsin, S., 1986, "Gravitational settling of aerosol particles in randomly oriented cellular flow fields," Journal of Atmospheric Sciences, **43**(11), pp. 1112–1134.

[4] Nielsen, P., 1993, "Turbulence effects on the settling of suspended particles," Journal of Sedimentary Research, **63**(5), pp. 835–838.

[5] Ingersoll, A. C., McKee, J. E., and Brooks, N. H., 1956, "Fundamental concepts of rectangular settling tanks," Transactions of the American Society of Civil Engineers, **121**(1), pp. 1179–1204.

[6] Murray, S. P., 1970, "Settling velocities and vertical diffusion of particles in turbulent water," Journal of Geophysical Research, **75**(9), pp. 1647–1654.

[7] Wang, M. R., Lian-Ping abd Maxey, 1993, "Settling velocity and concentration distribution of heavy particles in homogeneous isotropic turbulence," Journal of Fluid Mechanics, **256**, pp. 27–68.

[8] Wang, Q. and Squires, K., 1996, "Large eddy simulation of particle deposition in a vertical turbulent channel flow," International Journal of Multiphase Flow, **22**(4), pp. 667–683.

[9] Liu, J., Zhang, P., Wang, Z., Yuan, S., and Tang, H., 2021, "Interaction between dual spherical particles during settling in fluid," Physics of Fluids, **33**(1), p. 013312.

[10] Menter, F. R., 1994, "Two-equation eddy-viscosity turbulence models for engineering applications," AIAA Journal, **32**(8), pp. 1598–1605.

[11] Kajishima, T. and Takiguchi, S., 2002, "Interaction between particle clusters and particle-induced turbulence," International Journal of Heat and Fluid Flow, **23**(5), pp. 639–646.

[12] Burton, T. M. and Eaton, J. K., 2005, "Fully resolved simulations of particle-turbulence interaction," Journal of Fluid Mechanics, **545**, pp. 67–111.

[13] Burns, T., Davis, R., and Moore, E. F., 1999, "A pertubation study of particle dynamics in a plane wake flow," Journal of Fluid Mechanics, **384**, pp. 1–26.

[14] Haddadi, H., Shojaei-Zadeh, S., Connington, K., and Morris, J. F., 2014, "Suspension flow past a cylinder: Particle interactions with recirculating wakes," Journal of Fluid Mechanics, **760**, p. R2.

[15] Khosronejad, A., Rennie, C., Salehi Neyshabouri, S., and Townsend, R., 2007, "3D numerical modeling of flow and sediment transport in a laboratory channel bends," Journal of Hydraulic Engineering, **133**(10), pp. 1123–1134.

[16] Wilcox, D., 1991, "A half century historical review of the k-omega model," *29th aerospace sciences meeting*, DCW Industries, Inc., La Cañada, California, p. 615.

[17] Ivarson, M. M., 2021, "Numerical study of flow calming structures in hydropower plants," MSc thesis, NTNU.

[18] Daving, F., 2022, "Investigation of pressurized and open channel type sand trap of hydroelectric power plant," MSc thesis, NTNU.

[19] Næss, R., 2020, "CFD Simulations of Open and Closed Sand Trap Design for Tonstad Hydropower Plant," MSc thesis, NTNU.

[20] Steinkjer, S. M., 2018, "Hydraulic Scale Modeling of Sediments for Pressurized Sand Traps," MSc thesis, NTNU.

[21] Fergus, T., Hoseth, K., and Sæterbø, E., 2010, *Vassdragshåndboka: håndbok i vassdragsteknikk*.

[22] Chanson, H., 2004, *Environmental Hydraulics for Open Channel Flows*, Elsevier, ISBN: 0-7506-6165-8.

[23] Crowe, C., Chung, J., and Troutt, T., 1988, "Particle mixing in free shear flows," Progress in energy and combustion science, **14**(3), pp. 171–194.

[24] Cengel, Y. A. and Cimbala, J. M., 2018, *Fluid Mechanics: Fundamentals and applications*, 4th ed., McGraw-Hill Education, New York, ISBN: 978-1-259-69653-4.

[25] Bergman, T. L., Lavine, A. S., Incropera, F. P., and Dewitt, D. P., 2011, *Fundamentals of Heat and Mass Transfer*, 7th ed., John Wiley and Sons, Jefferson City, ISBN: 978-0470-50197-9.

[26] Subramaniam, S. and Balachandar, S., 2023, *Modeling Approaches and Computational Methods for Particle-laden Turbulent Flows*, 1st ed., Academic Press, Elsevier, London, ISBN: 978-0-323-90133-8.

[27] Bijan, M. and Pironneau, O., 1993, *Analysis of the k-epsilon turbulence model*, 1st ed., Editions MASSON, France, ISBN: 2-225-84391-0.

[28] Davidson, L., 2006, "Evaluation of the SST-SAS model: channel flow, asymmetric diffuser and axi-symmetric," Citeseer, European Conference of Computational Fluid Dynamics, p. 20.

[29] ANSYS, I., 23.02.2009, "18.1.1 Pressure-Based Solver," Last accessed: 20.04.2023, https://www.afs.enea.it/project/neptunius/docs/fluent/html/th/node361.htm

[30] Pope, S. B., 2000, *Turbulent flows*, ISBN: 0-521-59886-9.

[31] Davidson, L., 2006, "Evaluation of the SST-SAS model: channel flow, asymmetric diffuser and axi-symmetric hill," *European Conference on Computational Fluid Dynamics*, Citeseer, p. 20.

[32] ANSYS, Inc., 23.01.2009, "15. Discrete phase," Last accessed: 20.04.2023, https://www.afs.enea.it/project/neptunius/docs/fluent/html/th/node239.htm

[33] Adamczyk, W. P., Klimanek, A., Białecki, R. A., Węcel, G., Kozołub, P., and Czakiert, T., 2014, "Comparison of the standard Euler-Euler and hybrid Euler-Lagrange approaches for modeling particle transport in a pilot-scale circulating fluidized bed," Particuology, **15**, pp. 129–137.

[34] Betts, J. T. and Huffman, W. P., 1998, "Mesh refinement in direct transcription methods for optimal control," Optimal Control Applications and Methods, **19**(1), pp. 1–21.

[35] ANSYS, Inc., 29.01.2009, "6.2.2 Mesh Quality," Last accessed: 20.04.2022, https://www.afs.enea.it/project/neptunius/docs/fluent/html/ug/node167.htm

[36] Salim, S. M. and Cheah, S., 12009, "Wall y^+ strategy for dealing with wall-bounded turbulent flows," Proceedings of the international multiconference of engineers and computer scientists, **2**, pp. 2165–2170.

[37] Roache, P. J., 1994, "Perspective: a method for uniform reporting og grid refinement studies," Journal of fluids Engineering, **116**(3), pp. 405–413.

[38] Celik, I. B., Ghia, U., Roache, P. J., and Freitas, C. J., 2008, "Procedure for estimation and reporting of uncertainty due to discretization in CFD Applications," Journal of fluids Engineering - Transactions of the ASME, **130**(7).

[39] ANSYS, Inc., 23.02.2009, "18.1.1 Pressure-Based Solver," Last accessed: 13.05.2023, https://www.afs.enea.it/project/neptunius/docs/fluent/html/th/node361.htm

Appendices

Appendix A

A.1 Simulation and solution setup for GCI study

Table A.1: Simulation and solution setup for GCI study in Ansys Fluent.

Parameter	Description	Setting
General	Transient	
	Gravity	$g = 9.81$ m s^{-2}
Turbulence model	k-ω SST-SAS	
Materials	Solid particles	$\rho_p = 1.600 \times 10^3$ kg m^{-3}
	Incompressible fluid	$\rho = 9.982 \times 10^2$ kg m^{-3}
		$\nu = 1.003 \times 10^{-6}$ m^2 s^{-1}
Discrete phase	Two-way coupled	
	Particle diameter	$D = 0.0001$ m
	Injection interval	$t = [1, 2]$ s
Boundary conditions	Inlet	$U = 1.5$ m s^{-1}
	Cylinder walls	No-slip
	Top and bottom wall	No-slip
	Side walls	Free-shear
Method	Scheme	Coupled
	Pressure	Second order upwind
	Momentum	Bounded central differencing
	Turbulent kinetic energy	Second order
	Specific dissipation rate	Second order
	Transient formulation	Bounded second order implicit
Calculation	Total time	2 s
	Time step size	0.005 s
	Iterations	20

Appendices

Appendix B

B.1 Mechanical drawings of the models in the current study.

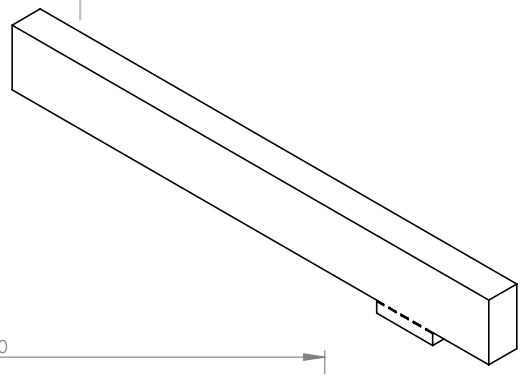

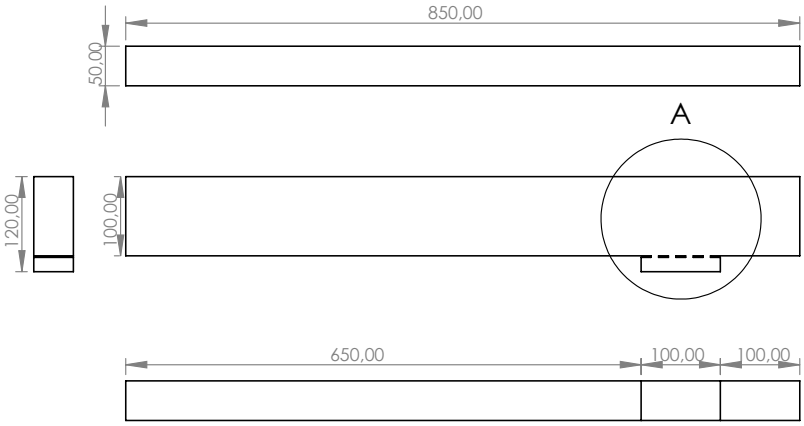

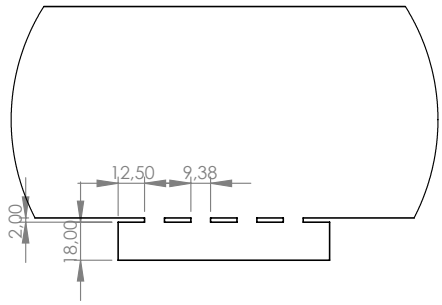

DETAIL A
SCALE 1 : 3

UNLESS OTHERWISE SPECIFIED: DIMENSIONS ARE IN MILLIMETERS SURFACE FINISH: TOLERANCES: LINEAR: ANGULAR:	FINISH:		DEBURR AND BREAK SHARP EDGES			DO NOT SCALE DRAWING	REVISION
		28.04.2023					

	NAME	SIGNATURE	DATE				TITLE:
DRAWN	**Model 1**	**Rebekka Stjern**	**28.04.23**				PART-15-DESC
CHK'D							
APPV'D							
MFG							
Q.A				MATERIAL:		DWG NO.	A4
						Model 1	
				WEIGHT:		SCALE:1:10	SHEET 1 OF 1

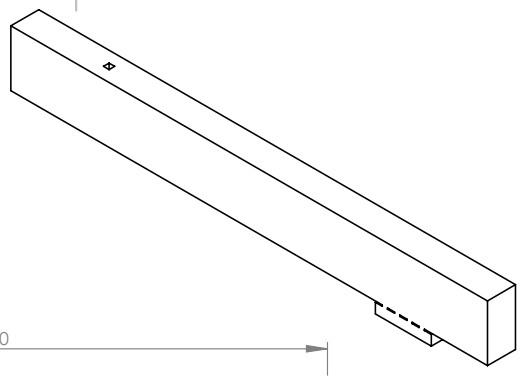

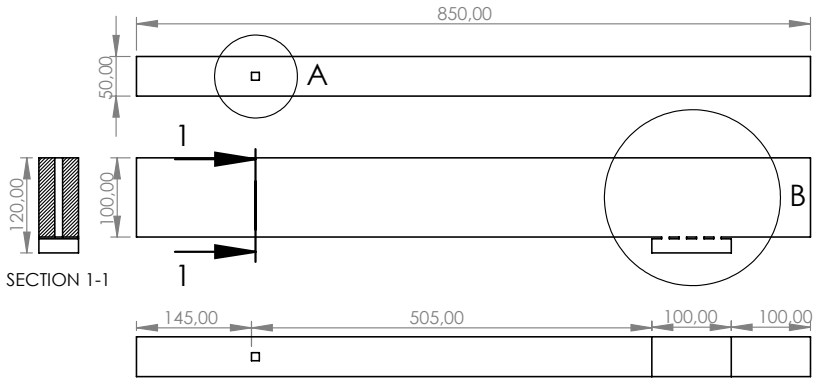

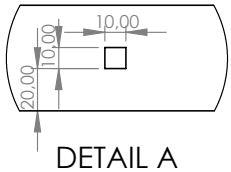

DETAIL A
SCALE 1 : 3

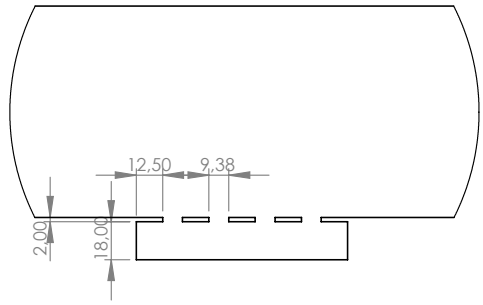

DETAIL B
SCALE 1 : 3

UNLESS OTHERWISE SPECIFIED: DIMENSIONS ARE IN MILLIMETERS SURFACE FINISH: TOLERANCES: LINEAR: ANGULAR:		FINISH:			DEBURR AND BREAK SHARP EDGES	DO NOT SCALE DRAWING	REVISION
		28.04.2023					
	NAME	SIGNATURE	DATE			TITLE:	
DRAWN	**Model 2**	**Rebekka Stjern**	**28.04.23**			PART-93-DESC	
CHK'D							
APPV'D							
MFG							
Q.A				MATERIAL:		DWG NO.	A4
						Model 2	
				WEIGHT:		SCALE:1:10	SHEET 1 OF 1

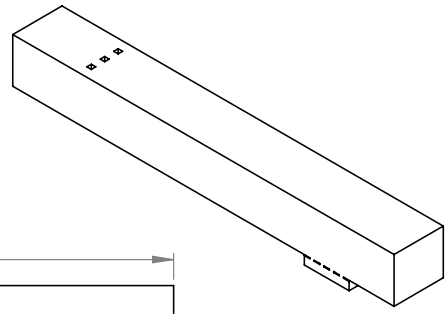

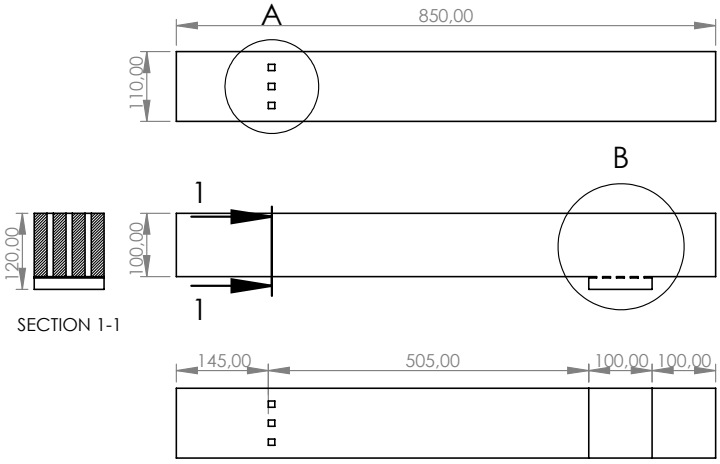

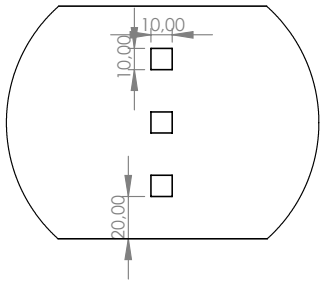

DETAIL A
SCALE 1 : 3

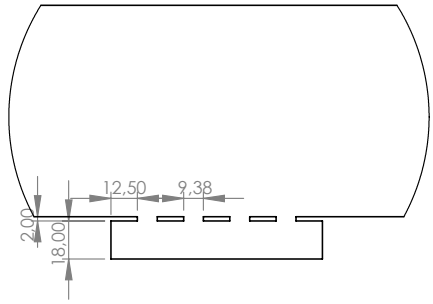

DETAIL B
SCALE 1 : 3

UNLESS OTHERWISE SPECIFIED: DIMENSIONS ARE IN MILLIMETERS SURFACE FINISH: TOLERANCES: LINEAR: ANGULAR:		FINISH:			DEBURR AND BREAK SHARP EDGES	DO NOT SCALE DRAWING	REVISION
		28.04.2023					
	NAME	SIGNATURE	DATE			TITLE:	
DRAWN	**Model 3**	**Rebekka Stjern**	**28.04.23**			PART-94-DESC	
CHK'D							
APPV'D							
MFG							
Q.A				MATERIAL:		DWG NO.	A4
						Model 3	
				WEIGHT:		SCALE:1:10	SHEET 1 OF 1

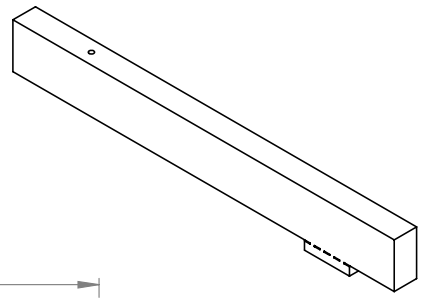

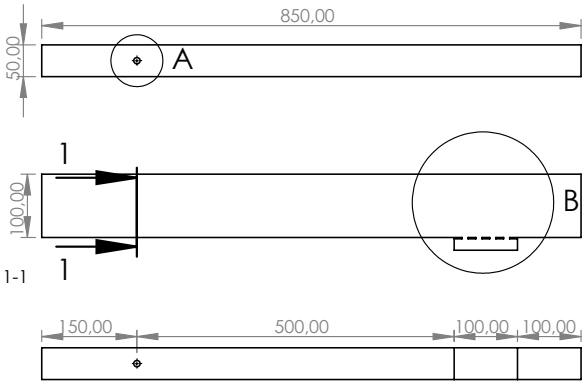

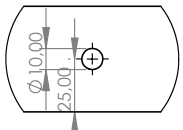

DETAIL A
SCALE 1 : 3

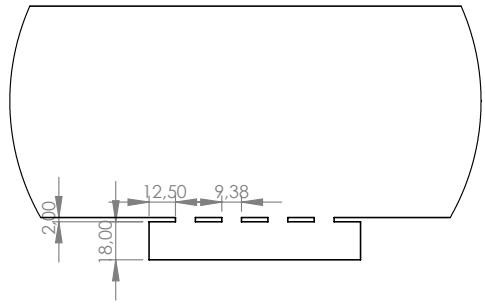

DETAIL B
SCALE 1 : 3

UNLESS OTHERWISE SPECIFIED: DIMENSIONS ARE IN MILLIMETERS SURFACE FINISH: TOLERANCES: LINEAR: ANGULAR:		FINISH:		DEBURR AND BREAK SHARP EDGES		DO NOT SCALE DRAWING	REVISION
		28.04.2023					
	NAME	SIGNATURE	DATE			TITLE:	
DRAWN	**Model 4**	**Rebekka Stjern**	**28.04.23**			PART-88-DESC	
CHK'D							
APPV'D							
MFG							
Q.A				MATERIAL:		DWG NO.	A4
						Model 4	
				WEIGHT:		SCALE:1:10	SHEET 1 OF 1

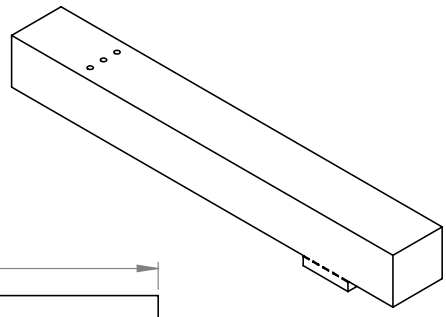

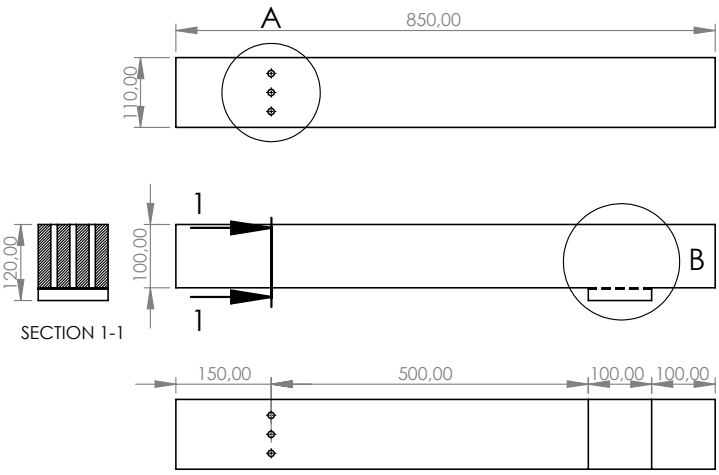

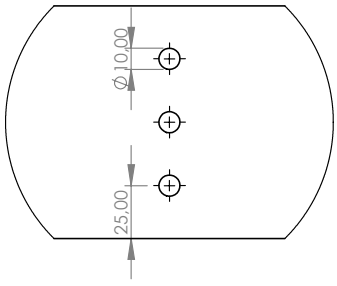

DETAIL A
SCALE 1 : 3

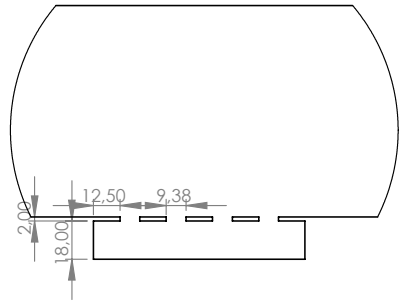

DETAIL B
SCALE 1 : 3

UNLESS OTHERWISE SPECIFIED: DIMENSIONS ARE IN MILLIMETERS SURFACE FINISH: TOLERANCES: LINEAR: ANGULAR:		FINISH:			DEBURR AND BREAK SHARP EDGES	DO NOT SCALE DRAWING	REVISION
		28.04.2023					
	NAME	SIGNATURE	DATE			TITLE:	
DRAWN	**Model 5**	**Rebekka Stjern**	**28.04.23**			PART-158-DESC	
CHK'D							
APPV'D							
MFG							
Q.A				MATERIAL:		DWG NO.	A4
						Model 5	
				WEIGHT:		SCALE:1:10	SHEET 1 OF 1

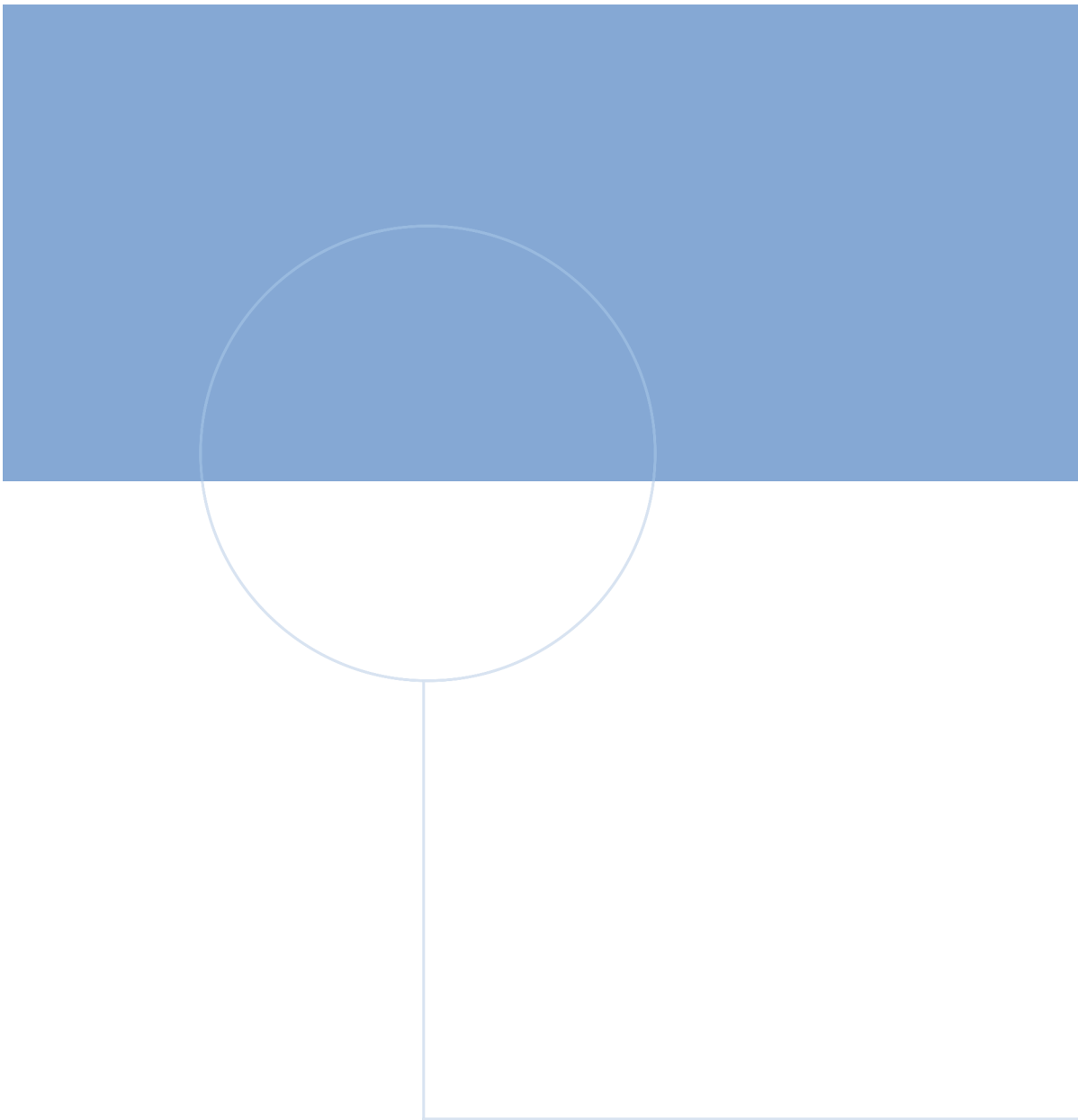

NTNU

Norwegian University of
Science and Technology